Eur. Phys. J. C (2012) 72:1973
DOI 10.1140/epjc/s10052-012-1973-6

THE EUROPEAN PHYSICAL JOURNAL C

Regular Article - Experimental Physics

Methods to determine neutrino flux at low energies

Investigation of the low ν method

A. Bodek[1,a], **U. Sarica**[1], **D. Naples**[2], **L. Ren**[2]

[1]Department of Physics and Astronomy, University of Rochester, Rochester, NY 14627-0171, USA
[2]University of Pittsburgh, Pittsburgh, PA 15260, USA

Received: 13 January 2012 / Revised: 21 March 2012 / Published online: 11 April 2012

Abstract We investigate the "low-ν" method (developed by the CCFR/NUTEV collaborations) to determine the neutrino flux in a wide band neutrino beam at very low energies, a region of interest to neutrino oscillations experiments. Events with low hadronic final state energy $\nu < \nu_{\rm cut}$ (of 1, 2 and 5 GeV) were used by the MINOS collaboration to determine the neutrino flux in their measurements of neutrino (ν_μ) and antineutrino ($\bar{\nu}_\mu$) total cross sections. The lowest ν_μ energy for which the method was used in MINOS is 3.5 GeV, and the lowest $\bar{\nu}_\mu$ energy is 6 GeV. At these energies, the cross sections are dominated by inelastic processes. We investigate the application of the method to determine the neutrino flux for ν_μ, $\bar{\nu}_\mu$ energies as low as 0.7 GeV where the cross sections are dominated by quasielastic scattering and $\Delta(1232)$ resonance production. We find that the method can be extended to low energies by using $\nu_{\rm cut}$ values of 0.25 and 0.50 GeV, which are feasible in fully active neutrino detectors such as MINERvA.

1 Introduction

A detailed understanding of neutrino (ν_μ) and antineutrino ($\bar{\nu}_\mu$) interaction cross sections for various final states is required for the next generation neutrino oscillations experiments. The relevant neutrino energy region of interest for the large neutrino detectors such as T2K [1], MINOS [2, 3], and NOVA [4] is $0.5 < E_\nu < 3$ GeV.

The MINERvA [5] experiment at the NUMI wide band beam at Fermilab uses a fine grain fully active scintillator target-detector to investigate neutrino (ν_μ) and antineutrino ($\bar{\nu}_\mu$) cross sections for energies above 0.5 GeV. These measurements require a reliable determination of the flux as a function of ν_μ, $\bar{\nu}_\mu$ energy.

Previous neutrino experiments in wide band beams used five methods for the determination of flux as a function of energy.

1. Modeling the distribution of pions and kaons produced by incident proton beam in the target. Then, tracking the pions and kaons though the Horn focussing magnetic fields, and modeling the decays of pions and kaons in the decay pipe.
2. Measuring the muon flux that exits the decay pipe and relating it to the neutrino flux.
3. Monitoring Inverse muon decay events ($\nu_\mu + e \rightarrow \mu^- + \nu_e$) in the detector.
4. Monitoring neutrino-electron scattering events ($\nu_\mu + e \rightarrow \nu_\mu + e$) in the detector.
5. The "low-ν" method for the determination of the energy dependence of the relative neutrino and antineutrino flux.

Here, "low-ν" [6, 7] refers to events with low energy transfer to the target nucleon in the scattering processes $\nu_\mu + N \rightarrow \mu^- + X$ and $\bar{\nu}_\mu + N \rightarrow \mu^+ + X$. This energy transfer manifests itself as the energy ($\nu = E_{\rm had}$) of the final state hadrons (X) in the laboratory frame.

There are inherent difficulties in the each of those techniques:

1. In method 1, the differential cross sections for the production of pions and kaons by protons incident on a thick nuclear target must be known very well. In addition, the magnetic field of the horn focussing magnets must be modeled reliably.
2. In method 2, the response of the muon detectors at the end of the decay pipe must be very well understood (for absolute calibration of the neutrino flux). The response of the muon detectors is sensitive to δ rays. In

[a] e-mail: bodek@pas.rochester.edu

addition, since the energy of the muons is not measured, it is difficult to determine the energy dependence of the neutrino flux.

3. In method 3, the threshold for the reaction $\nu_\mu + e \to \mu^- + \nu_e$ is about 12 GeV. Therefore, this method can only be used at higher energies. Unfortunately, this method cannot be used for the determination of the flux for antineutrinos. Inverse muon decay was used by NOMAD to constrain their neutrino flux at high energies.
4. In method 4, only the sum of the fluxes for neutrinos and antineutrinos can be measured. This is because calorimetric detectors such as MINERvA cannot determine the charge of final state electron in $\nu_\mu + e \to \nu_\mu + e$ events.

Both methods 4 and 5 are statistically limited. In addition, in both methods, the total final state energy in the events is not fully reconstructed since there is a neutrino in the final state. This places a limitation on the determination of the energy dependence of the neutrino and antineutrino fluxes. Despite of these limitations, these two additional methods are valuable as important consistency checks.

Consequently, having another independent technique such as the "low-ν" method is extremely valuable.

The "low-ν" method was initially developed by the CCFR/NuTeV [6, 7] collaboration. At high energy, the method was used to determine the relative neutrino flux as a function of neutrino energy (E_ν). The method relies on the observation that the charged current differential cross section, $\frac{d\sigma^{\nu,\bar\nu}}{d\nu}$ in the limit $\nu \to 0$, only depends on the structure function $\mathcal{F}_2$, and therefore is independent of energy.

The "low-ν" method was used by the CCFR/NuTeV collaborations to measure the energy dependence of σ_ν/E and $\sigma_{\bar\nu}/E$ for charged current interactions for energies higher than 30 GeV for an iron target. The absolute level of the charged cross sections is normalized to previous measurements of σ_ν/E in a high energy narrow band neutrino beam.

Most recently, the method was extended to lower energies by the MINOS [3] collaboration. The lowest neutrino energy for which this method was used in MINOS is 3.5 GeV for neutrinos and 6 GeV for antineutrinos.

The absolute normalization used by MINOS is to the world average value of charged current σ_ν/E measurements for an isoscalar target for neutrino energies between 30 to 50 GeV. The average value used by MINOS is

$$\langle \sigma_\nu/E \rangle_{30-50} = 0.675 \times 10^{-38}\ \mathrm{cm}^2/\mathrm{GeV}$$

per nucleon. The antineutrino sample is not independently normalized but is related to the neutrinos by using the same normalization factor.

In this communication we investigate the application of the technique to much lower neutrino energies ($E_\nu > 0.5$ GeV). Neutrino interactions in this energy range are currently being studied at MINERvA.

2 The "low-ν" method at high energies

If we neglect terms which are proportional to the muon mass, the differential cross section $\frac{d^2\sigma^{\nu,\bar\nu}}{dx\,dy}$ for charged current scattering of ν_μ ($\bar\nu_\mu$) with an incident energy E_ν, muon final energy E_μ and scattering angle θ can be written in terms of the structure functions $\mathcal{F}_1 = M\mathcal{W}_1(x, Q^2)$, $\mathcal{F}_2 = \nu\mathcal{W}_2(x, Q^2)$ and $\mathcal{F}_3 = \nu\mathcal{W}_3(x, Q^2)$:

$$\frac{d^2\sigma^{\nu(\bar\nu)}}{dx\,dy} = \frac{G_F^2 M E_\nu}{\pi}\left(\left[1 - y\left(1 + \frac{Mx}{2E_\nu}\right) + \frac{y^2}{2}\left(\frac{1 + (\frac{2Mx}{Q})^2}{1+R}\right)\right]\mathcal{F}_2 \pm \left[y - \frac{y^2}{2}\right]x\mathcal{F}_3\right), \tag{1}$$

where G_F is the Fermi weak coupling constant, M is the proton mass, $y = \nu/E_\nu$, $\nu = E_{\mathrm{had}} = E_\nu - E_\mu$, $Q^2 = 4E_\nu E_\mu \sin^2(\theta/2)$ is the square of four momentum transfer, and $x = Q^2/(2M\nu)$ is the Bjorken scaling variable. The plus sign in front of the xF_3 term is for neutrinos and the minus is for antineutrinos.

Here, $R(x, Q^2)$ is defined as the ratio of the longitudinal and transverse structure functions (σ_L/σ_T). It is related to the other structure functions by,

$$R(x, Q^2) = \frac{\sigma_L}{\sigma_T} = \frac{\mathcal{F}_2}{2x\mathcal{F}_1}\left(1 + \frac{4M^2x^2}{Q^2}\right) - 1 = \frac{\mathcal{F}_L}{2x\mathcal{F}_1}, \tag{2}$$

where $\mathcal{F}_L$ is called the longitudinal structure function,

$$\mathcal{F}_L(x, Q^2) = \mathcal{F}_2\left(1 + \frac{4M^2x^2}{Q^2}\right) - 2x\mathcal{F}_1. \tag{3}$$

Other useful relations are:

$$2x\mathcal{F}_1(x, Q^2) = \mathcal{F}_2(x, Q^2)\frac{1 + 4M^2x^2/Q^2}{1 + R(x, Q^2)}, \tag{4}$$

$$\mathcal{W}_1(x, Q^2) = \mathcal{W}_2(x, Q^2)\frac{1 + \nu^2/Q^2}{1 + R(x, Q^2)}.$$

The three structure functions $\mathcal{F}_2(x, Q^2)$, $\mathcal{F}_1(x, Q^2)$ and $x\mathcal{F}_3(x, Q^2)$ depend on x and Q^2.

Integrating over x, the differential dependence on ν can be written in the simplified form

$$\frac{d\sigma^{\nu,\bar\nu}}{d\nu} = A\left(1 + \frac{B}{A}\frac{\nu}{E_\nu} - \frac{C}{A}\frac{\nu^2}{2E_\nu^2}\right). \tag{5}$$

The coefficients A, B, and C depend on integrals over structure functions, where

$$A = \frac{G_F^2 M}{\pi}\int_0^1 \mathcal{F}_2(x)\,dx,$$
$$B = -\frac{G_F^2 M}{\pi}\int_0^1 \left(\mathcal{F}_2(x) \mp x\mathcal{F}_3(x)\right)dx, \tag{6}$$
$$C = B - \frac{G_F^2 M}{\pi}\int_0^1 \mathcal{F}_2(x)\tilde{R}\,dx,$$

and

$$\tilde{R} = \left(\frac{1 + \frac{2Mx}{\nu}}{1 + R(x, Q^2)} - \frac{Mx}{\nu} - 1 \right).$$

In the limit $\nu/E_\nu \to 0$, the A term dominates and the B and C terms are very small. The MINOS collaboration used the number of "low-ν" events (with $\nu < \nu_{\rm cut}$) in the detector to determine the relative flux of neutrinos and antineutrinos as a function of E_ν.

In the MINOS analysis, the relative flux is determined using events with $\nu < 1$ GeV for ν_μ energies in the range $3 < E_\nu < 9$ GeV, and for $\bar{\nu}_\mu$ in the range $5 < E_\nu < 9$ GeV. Events with $\nu < 2$ GeV are used for ν_μ and $\bar{\nu}_\mu$ events in the range $9 < E_\nu < 18$ GeV, and events with $\nu < 5$ GeV are used for $E_\nu > 18$ GeV.

MINOS divides the number of "low-ν" events with $y < y_{\rm cut} = \nu_{\rm cut}/E_\nu$ by correction term f_C to account for the energy dependence from the B and C terms. Here

$$f_C(E_\nu) = 1 + \int_0^{y_{\rm cut}} \frac{B}{A} \frac{\nu}{E_\nu} dy - \int_0^{y_{\rm cut}} \frac{C}{A} \frac{\nu^2}{2E_\nu^2} dy. \tag{7}$$

As seen in equation (6), the negative contribution of $\mathcal{F}_2(x)$ in B partially cancels the positive contribution of $x\mathcal{F}_3(x)$ for ν_μ's. For $\bar{\nu}_\mu$'s both contributions are negative. There are additional small corrections that are applied to equation (6) to correct for differences in $\mathcal{F}_2$ between neutrinos and antineutrinos.

In practice, a neutrino interaction generator model [8] is used to compute f_C from

$$f_C(E_\nu) = \frac{\sigma(\nu < \nu_{\rm cut}, E_\nu)}{\sigma(\nu < \nu_{\rm cut}, E_\nu = \infty)}. \tag{8}$$

The corrections factors f_C used by MINOS for ν_μ and $\bar{\nu}_\mu$ are shown in Fig. 1.

The measured "low-ν" sample is corrected for detector smearing and acceptance by multiplying the number of observed "low-ν" events in the data in each energy bin by

$$R^{\rm MC}(E_\nu) = \frac{N^{\rm GEN}(E_{\rm reconstructed}, \nu < \nu_{\rm cut})}{N^{\rm REC}(E_{\rm reconstructed}, \nu < \nu_{\rm cut})},$$

which is obtained from a Monte Carlo detector simulation. $N^{\rm GEN}$ and $N^{\rm REC}$ are the number of generated and reconstructed events below $\nu_{\rm cut}$ in each reconstructed energy bin, respectively. In the first pass the initial input flux from a beam model is used. It is then replaced by the extracted "low-ν" flux and the procedure is reiterated to account for the effect of the flux model on the acceptance corrections. (The change in the extracted flux is found to be negligible). The "low-ν" sample is further corrected for radiative effects using Ref. [9]. The absolute level of the flux is set by normalizing the cross section in data to a nominal world average charged current cross section at some high energy. As mentioned earlier, in MINOS the normalization is set to the average of previous $\sigma_{\rm total}/E$ measurements for neutrino energies between 30 and 50 GeV.

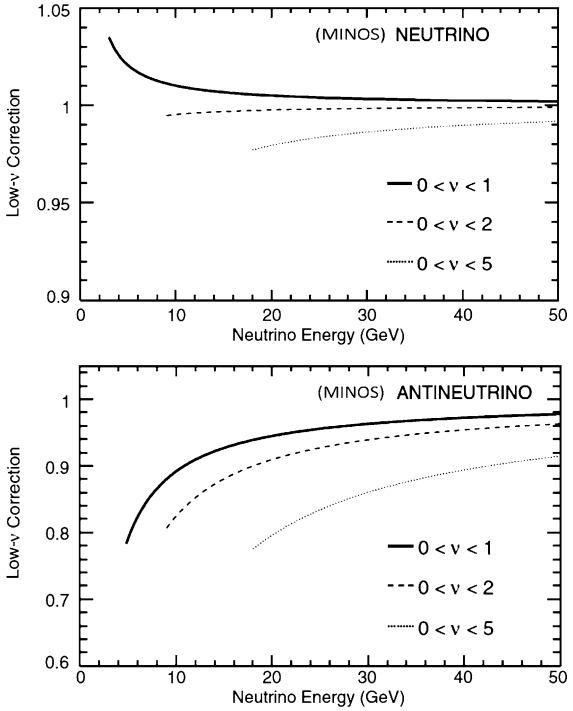

Fig. 1 The "low-ν" correction factors f_C used by MINOS for neutrinos (shown in the *top panel*) and antineutrinos (shown in the *bottom panel*)

There are three criteria for the effectiveness of the "low-ν" method.

1. The number of "low-ν" events that are used in the determination of the flux should not be a large fraction of the total number of neutrino events in each energy bin.
2. The systematic uncertainty in the energy dependent correction factor f_C should be small.
3. The number of "low-ν" events that are used in the determination of the flux should be sufficiently large to have flux sample with small statistical errors.

The first two criteria require a $\nu_{\rm cut}$ which is as low as possible. The third requires a $\nu_{\rm cut}$ which is as large as possible.

The MINOS collaboration uses the criteria that the fractional contribution of events with $\nu < \nu_{\rm cut}$ to the total charged current cross section should be less than 60 %. MINOS uses events with $\nu < 1$ GeV for determination of the flux at their lowest ν_μ, $\bar{\nu}_\mu$ energies.

The fraction of events with $\nu < 1$ GeV is less than 60 % for ν_μ interactions with $E_\nu > 3$ GeV and for $\bar{\nu}_\mu$ interactions with $E_{\bar{\nu}} > 5$ GeV. Therefore, to determine the flux for $E_\nu < 3$ GeV and $E_{\bar{\nu}} < 5$ GeV we need to use a $\nu_{\rm cut}$ which is smaller than 1 GeV.

We investigate $\nu_{\rm cut} = 0.25$ GeV to be used for $E_{\nu,\bar{\nu}} > 0.7$ GeV, and $\nu_{\rm cut} = 0.5$ GeV to be used for $E_{\nu,\bar{\nu}} > 1.4$ GeV. These samples can be cross calibrated against the $\nu_{\rm cut} = 1$ GeV sample in the range $E_\nu > 3$ GeV for neutrinos and

$E_{\bar{\nu}} > 5$ GeV for antineutrinos. Similarly, they can be calibrated against the $\nu_{\rm cut} = 2$ GeV and $\nu_{\rm cut} = 5$ GeV samples in the range $E_{\nu,\bar{\nu}} > 9$ GeV and $E_{\nu,\bar{\nu}} > 18$ GeV, respectively.

3 The "low-ν" method at low energies

In the few GeV region, there are several types of neutrino interaction processes as defined by the final state invariant mass W. These include quasielastic (QE) reactions ($W < 1.07$ GeV), production of the $\Delta(1232)$ resonance ($1.1 < W < 1.4$ GeV), coherent pion production, production of higher mass resonances ($1.4 < W < 2.0$ GeV) and the inelastic continuum ($W > 2.0$ GeV). Figure 2 shows the kinematic region in Q^2 (in GeV^2) and $\nu = E_{\rm had}$ (in GeV) for $E_\nu < 4$ GeV.

Figure 3 shows the kinematic region in Q^2 and ν for $E_\nu < 1.5$ GeV. In this paper we focus on $\nu < 0.25$ GeV region (shaded area in Figs. 2 and 3) for the lowest neutrino energies. In addition, we investigate the $\nu < 0.50$ GeV region as an additional check.

For $E_\nu = 3$ GeV, about 1/3 of the total charged current cross section originates from QE scattering, 1/3 from resonance production and 1/3 from inelastic scattering.

As seen in Fig. 3 the $\nu < 0.25$ GeV sample is dominated almost entirely by QE events with $Q^2 < 0.45$ GeV^2.

The $\nu < 0.5$ GeV sample includes both QE events with $Q^2 < 0.95$ GeV^2 and also $\Delta(1232)$ resonance events with $Q^2 < 0.3$ GeV^2. Both samples include a very small fraction of events originating from coherent pion production (as discussed in Appendix B).

In the very "low-ν" region it is more convenient to write the expression for the charged current differential cross sections as follows [10–13]:

$$\begin{aligned}\frac{d^2\sigma}{dQ^2 d\nu} &= S_{\cos}\frac{1}{2E^2}\mathcal{W}_1\left[Q^2 + m_\mu^2\right] \\ &\quad + S_{\cos}\mathcal{W}_2\left[\left(1 - \frac{\nu}{E}\right) - \frac{(Q^2 + m_\mu^2)}{4E^2}\right] \\ &\quad + S_{\cos}\mathcal{W}_3\left[\frac{Q^2}{2ME} - \frac{\nu}{4E}\frac{Q^2 + m_\mu^2}{ME}\right] \\ &\quad + S_{\cos}\mathcal{W}_4\left[m_\mu^2\frac{(Q^2 + m_\mu^2)}{4M^2E^2}\right] \\ &\quad - S_{\cos}\mathcal{W}_5\left[\frac{m_\mu^2}{ME}\right], \end{aligned} \tag{9}$$

where $S_{\cos} = \frac{G^2}{2\pi}\cos^2\theta_C = 80 \times 10^{-40}$ cm^2/GeV^2. In the scattering process, there are additional small contributions from strangeness and charm non-conserving processes. In the discussion below we do not show these terms explicitly, but charm and strangeness changing contributions are assumed to be included in the analysis. (The strangeness changing valence quark contributions are proportional to $\frac{G^2}{2\pi}\sin^2\theta_C$.)

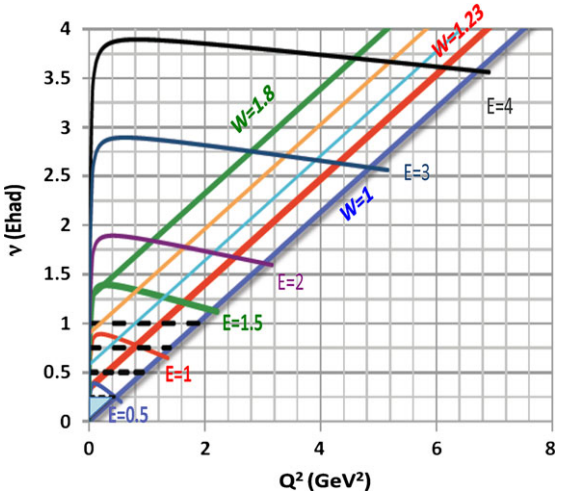

Fig. 2 The kinematic region in the Q^2 (in GeV^2), $\nu = E_{\rm had}$ (in GeV) plane for ν_μ ($\bar{\nu}_\mu$) energies less than 4 GeV. The *shaded area* is $\nu <$ 0.25 GeV (Color figure online)

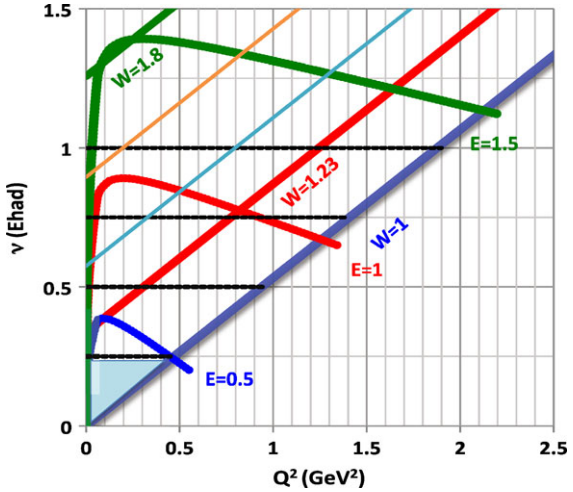

Fig. 3 The kinematic region in the Q^2 (in GeV^2), $\nu = E_{\rm had}$ (in GeV) plane for ν_μ ($\bar{\nu}_\mu$) energies less than 1.5 GeV. The *shaded area* is $\nu <$ 0.25 GeV (Color figure online)

Each of the structure functions has a vector and axial component (except for $\mathcal{W}_3$ which originates from axial-vector interference). The vector part of $\mathcal{W}_4$ and $\mathcal{W}_5$ are well known since they are related to the vector part of $\mathcal{W}_2$ and $\mathcal{W}_1$ by the following expressions [10–12]:

$$\mathcal{W}_4^{\rm vector} = \mathcal{W}_2^{\rm vector}\frac{M^2\nu^2}{Q^4} - \mathcal{W}_1^{\rm vector}\frac{M^2}{Q^2},$$

$$\mathcal{W}_5^{\rm vector} = \mathcal{W}_2^{\rm vector}\frac{M\nu}{Q^2}.$$

At 'low-ν' and very high energy the charged current cross section is only a function of $\mathcal{W}_2$. If we integrate the cross section from $\nu_{\rm min} \approx 0$ up to $\nu = \nu_{\rm cut}$ (where $\nu_{\rm cut}$ is small),

we can write the expression for the cross section in terms of $\mathcal{W}_2$ only, and energy dependent corrections ratios to the $\mathcal{W}_2$ component:

$$\sigma_{\nu\text{cut}}(E) = \int_{\nu_{\min(E)}}^{\nu_{\text{cut}}} \frac{d^2\sigma}{dQ^2 d\nu}\, dQ^2\, d\nu = \sigma_{W_2} + \sigma_2 + \sigma_1 + \sigma_3 + \sigma_4 + \sigma_5. \tag{10}$$

Here, $\sigma_{W_2} \approx \sigma_{W_2}(\infty)$, where

$$\sigma_{W_2} = S_{\cos} \int_{\nu_{\min(E)}}^{\nu_{\text{cut}}} \mathcal{W}_2\, d\nu, \tag{11}$$

$$\sigma_{W_2}(\infty) = S_{\cos} \int_{\nu_{\min(E=\infty)}}^{\nu_{\text{cut}}} \mathcal{W}_2\, d\nu, \tag{12}$$

and the small corrections to the QE cross section are:

$$\begin{aligned}
\sigma_2 &= S_{\cos} \int_{\nu_{\min(E)}}^{\nu_{\text{cut}}} \left[-\frac{\nu}{E} - \frac{Q^2+m_\mu^2}{4E^2}\right]\mathcal{W}_2\, d\nu,\\
\sigma_1 &= S_{\cos} \int_{\nu_{\min(E)}}^{\nu_{\text{cut}}} -\left[\frac{(Q^2+m_\mu^2)}{2E^2}\right]\mathcal{W}_1\, d\nu,\\
\sigma_3 &= S_{\cos} \int_{\nu_{\min(E)}}^{\nu_{\text{cut}}} \left[\frac{Q^2}{2ME} - \frac{\nu}{4E}\frac{Q^2+m_\mu^2}{ME}\right]\mathcal{W}_3\, d\nu,\\
\sigma_4 &= S_{\cos} \int_{\nu_{\min(E)}}^{\nu_{\text{cut}}} \left[m_\mu^2 \frac{(Q^2+m_\mu^2)}{4M^2E^2}\right]\mathcal{W}_4\, d\nu,\\
\sigma_5 &= S_{\cos} \int_{\nu_{\min(E)}}^{\nu_{\text{cut}}} \left[\frac{-m_\mu^2}{ME}\right]\mathcal{W}_5\, d\nu.
\end{aligned} \tag{13}$$

The above can be written in terms of fractional corrections:

$$\begin{aligned}
&\sigma_{\nu\text{cut}}(E) = \sigma_{W_2}(\infty)[f_C],\\
&f_C = [f_{W2} + f_2 + f_1 + f_3 + f_4 + f_5],\\
&f_{W2} = \frac{\sigma_{W2}}{\sigma_{W_2}(\infty)} \approx 1,\\
&f_i = \frac{\sigma_i}{\sigma_{W_2}(\infty)}.
\end{aligned} \tag{14}$$

The energy dependent corrections f_{W2}, f_1, f_2, f_3, f_3, and f_4 and f_5 can be calculated within a specific models. The theoretical uncertainty in f_C determines the systematic uncertainty in the relative flux which can extracted from the "low-ν" events.

1. $f_{W2} = \frac{\sigma_{W2}}{\sigma_{W_2}(\infty)} \approx 1$ is well known and does not contribute to the uncertainty in f_C.
2. The energy dependent correction f_2 is explicit and therefore does not contribute to the uncertainty in f_C.
3. The contributions of f_4 and f_5 are small since they are proportional to the square of the muon mass, and therefore have a negligible contribution to the uncertainty in f_C. (Note that the vector parts of f_4 and f_5 are known very well since they can be expressed in terms of the vector parts of $\mathcal{W}_1$ and $\mathcal{W}_2$.)

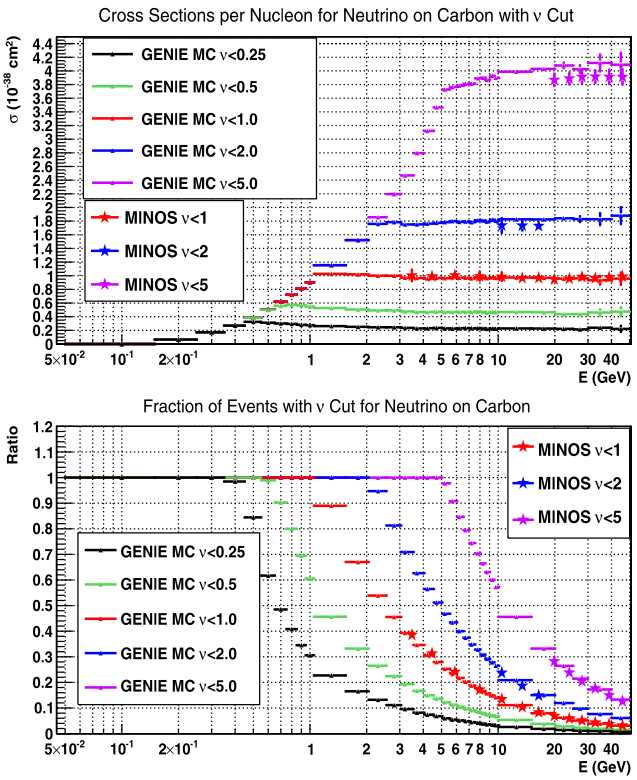

Fig. 4 *Top panel*: Neutrino partial charged cross sections per nucleon for "low-ν" events determined from the GENIE Monte Carlo [14–17]. Also shown are the measurements of MINOS on iron (per nucleon corrected for the excess number of neutrons). *Bottom panel*: The fraction of "low-ν" neutrino events in the GENIE [14–17] Monte Carlo as compared with the measurements of MINOS (Color figure online)

4. The only non-negligible uncertainty originates from the modeling of the contributions of f_1 and f_3 (primarily from f_3).

The technique does not depend on the modeling of $\mathcal{W}_2$ because the σ_{W_2} cross section is the same at all energies. All energy dependent corrections are expressed in terms of ratios to σ_{W_2}. In quark parton language, the uncertainty in f_1 is related to the uncertainty in the longitudinal structure function at low Q^2 and the uncertainty in f_3 is related to the uncertainty in level of antiquarks in the nucleon at low Q^2. For QE scattering and resonance production the structure functions are expressed in terms of form factors.

3.1 Partial charged current cross sections

The top panel of Fig. 4 shows the partial neutrino charged current cross section per nucleon for "low-ν" events (for ν cuts of 0.25, 0.5, 1, 2 and 5 GeV) as a function of energy as determined by the GENIE [14–17] Monte Carlo for a carbon target. The top panel of Fig. 5 shows the corresponding partial charged current cross sections for antineutrinos.

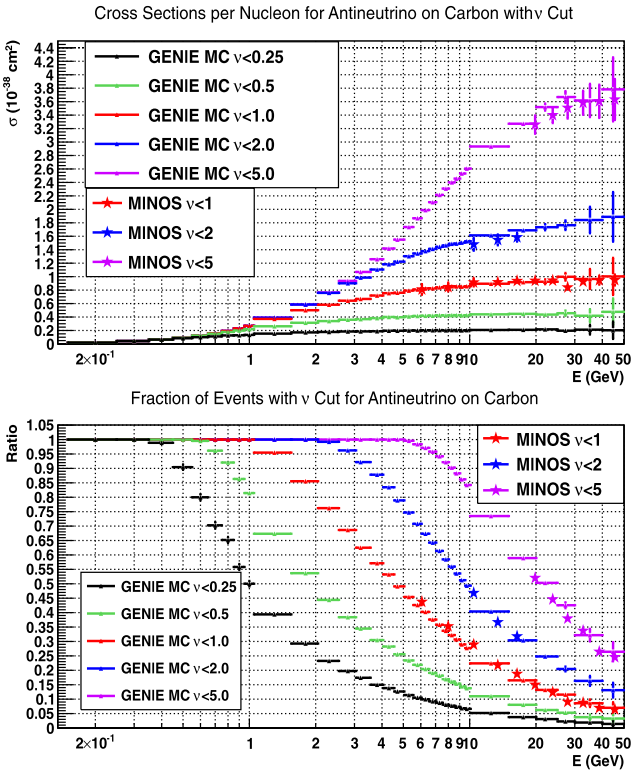

Fig. 5 Same as Fig. 4 for the case of antineutrinos (Color figure online)

Also shown are the measurements of the partial charged current cross sections on iron from the MINOS collaboration (for ν cuts of 1, 2 and 5 GeV). The MINOS cross sections for iron have been corrected for the excess number of neutrons in iron. Note that the nuclear corrections to the structure functions in iron nucleus are larger than in carbon. Therefore, the partial cross sections on carbon and on iron may not be the same.

At high energies (as shown in Figs. 4 and 5) the partial cross sections for a fixed ν_{cut} are independent of energy and are approximately equal for neutrinos and antineutrino. The fact that these partial charged current cross section are relatively independent of energy is the basis for the "low-ν" method.

The bottom panels of Figs. 4 and 5 show the fraction of "low-ν" events predicted by the GENIE Monte Carlo as compared with the measurements in MINOS. In order to use the technique at low energies the fractions must be smaller than 0.6. Therefore, at the lowest energies we must use ν cuts of 0.25 and 0.50 GeV.

MINOS is a sampling target calorimeter which has poor resolution at low hadron energy. Therefore, "low-ν" samples with $\nu < 0.25$ GeV and $\nu < 0.5$ GeV cannot be defined reliably. On the other hand, since the MINERvA detector is a fully active target calorimeter, "low-ν" samples with $\nu < 0.25$ GeV and $\nu < 0.5$ GeV can be used.

3.2 Absolute normalization

Since the neutrino energy range for MINERvA is limited to lower energies, we propose that the MINERvA charged current cross section measurements be normalized to the cross section in the energy range between 10 to 20 GeV (e.g. at a mean energy of 15.1 GeV). The absolute level of the charged current cross section at this energy range has been measured by both the MINOS and NOMAD collaborations.

The MINOS total cross section measurement for an isoscalar iron target at a neutrino energy of 15.1 GeV is

$$\sigma_{\nu}^{\mathrm{MINOS}}/E = 0.708 \pm 0.020 \times 10^{-38}\ \mathrm{cm}^2/\mathrm{GeV}$$

per nucleon in iron. Here the total error of 0.02 is the combined statistical, systematic and normalization errors of $0.008 \pm 0.012 \pm 0.015$, respectively.

The NOMAD cross section measurement for an isoscalar carbon target at a neutrino energy of 15.1 GeV is

$$\sigma_{\nu}^{\mathrm{NOMAD}}/E = 0.698 \pm 0.025 \times 10^{-38}\ \mathrm{cm}^2/\mathrm{GeV}$$

per nucleon in carbon.

The MINOS total cross section measurement for an isoscalar iron target at an antineutrino energy of 15.1 GeV is

$$\sigma_{\bar{\nu}}^{\mathrm{MINOS}}/E = 0.304 \pm 0.012 \times 10^{-38}\ \mathrm{cm}^2/\mathrm{GeV}$$

per nucleon in iron. Here, the total error of 0.012 is the combined statistical, systematic and normalization errors of $0.007 \pm 0.007 \pm 0.006$, respectively.

Alternatively, it may be possible for MINERvA to normalize to the partial cross sections measured by MINOS for $\nu < 1$ GeV and $\nu < 2$ GeV at 15.1 GeV. These partial cross sections (which were used by MINOS to determine their relative flux) are relatively constant between 10 and 20 GeV. However, the MINOS partial cross sections are measured on iron. The MINERvA target is solid scintillator (i.e. carbon), and the partial cross sections for iron and carbon can be different. For a neutrino energy of 15.1 GeV MINOS measured the following isoscalar partial cross sections on iron (per nucleon):

$$\sigma_{\nu}^{\mathrm{MINOS}}(15.1) = 1.729 \pm 0.049 \times 10^{-38}\,\mathrm{cm}^2 \quad (\nu < 2\,\mathrm{GeV}),$$

$$\sigma_{\nu}^{\mathrm{MINOS}}(15.1) = 0.968 \pm 0.027 \times 10^{-38}\,\mathrm{cm}^2 \quad (\nu < 1\,\mathrm{GeV}).$$

For an antineutrino energy of 15.1 GeV MINOS has measured the following isoscalar partial cross sections:

$$\sigma_{\bar{\nu}}^{\mathrm{MINOS}}(15.1) = 1.585 \pm 0.063 \times 10^{-38}\,\mathrm{cm}^2 \quad (\nu < 2\,\mathrm{GeV}),$$

$$\sigma_{\bar{\nu}}^{\mathrm{MINOS}}(15.1) = 0.939 \pm 0.039 \times 10^{-38}\,\mathrm{cm}^2 \quad (\nu < 1\,\mathrm{GeV}).$$

4 Using "low-ν" events with $\nu < 0.25$ GeV

As seen in Fig. 3 the $\nu < 0.25$ GeV region is dominated by QE events. This is illustrated in Fig. 6 which shows the relative contributions of QE and non-QE processes to $\nu < 0.25$ GeV cross section as a function of energy (as determined from the GENIE Monte Carlo). The $\nu < 0.25$ GeV cross sections for ν_μ are shown on the top panel, and the $\nu < 0.25$ GeV cross sections for $\bar{\nu}_\mu$ are shown on the bottom panel. The QE contribution is shown in red, the contribution from pion production process (e.g. Δ, inelastic and coherent pion) is shown in blue and the total is shown in black. Most of the events are QE and the contribution from pion production processes is negligible.

As mentioned earlier, the technique does not rely on the modeling of $\mathcal{W}_2$, or the modeling of nuclear effects (e.g. Fermi motion smearing) on $\mathcal{W}_2$. This is because the cross section σ_{W_2} (including nuclear effects) is the same at all neutrino energies.

The uncertainty in the flux extracted from the event sample with $\nu < 0.25$ GeV is determined by how well we can model the relative contributions of $\mathcal{W}_1$ and $\mathcal{W}_3$ for the case of QE scattering on bound nucleons, or equivalently the relative contributions of f_1 and f_3 to f_C. Here f_1 and f_3 are proportional to the ratios $\frac{\mathcal{W}_1}{\mathcal{W}_2}$ and $\frac{\mathcal{W}_3}{\mathcal{W}_2}$. Since the ratios $\frac{\mathcal{W}_1}{\mathcal{W}_2}$ and $\frac{\mathcal{W}_3}{\mathcal{W}_2}$ for QE scattering on free nucleons are very well known, the uncertainty in f_C originates primarily from modeling the nuclear corrections to $\frac{\mathcal{W}_1}{\mathcal{W}_2}$ and $\frac{\mathcal{W}_3}{\mathcal{W}_2}$ for nucleons bound in a nuclear target.

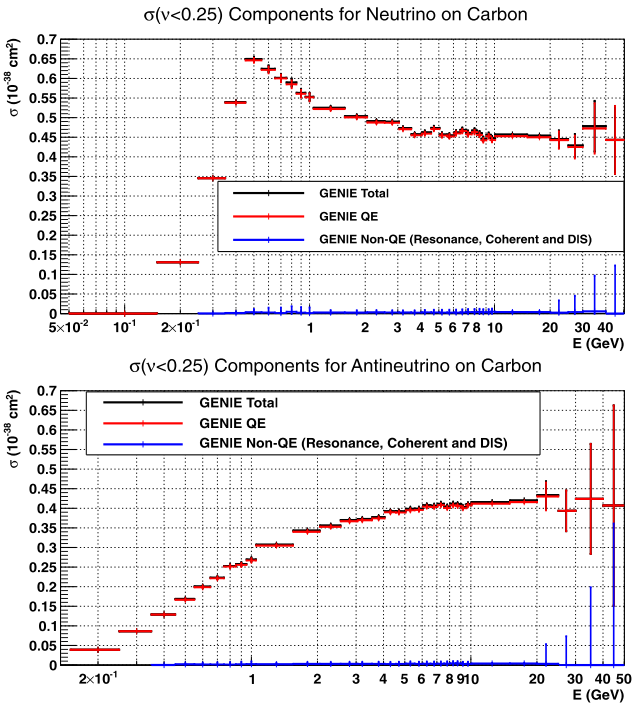

Fig. 6 The $\nu < 0.25$ GeV partial charged current cross sections (per nucleon) as a function of energy from the GENIE Monte Carlo (for carbon target). Shown are the QE contribution, the contribution from pion production process (e.g. Δ, inelastic and coherent pion) and the total. The $\nu < 0.25$ GeV cross sections for ν_μ are shown on the *top panel*, and the $\nu < 0.25$ GeV cross sections for $\bar{\nu}_\mu$ are shown on the *bottom panel* (Color figure online)

4.1 Quasielastic $\nu_\mu, \bar{\nu}_\mu$ scattering

The relationship between the structure functions and form factors for $\nu_\mu, \bar{\nu}_\mu$ QE scattering [18, 19] on free nucleons is given by [20, 21]:

$$W_{1\text{-Qelastic}}^{\nu\text{-vector}} = \delta\left(\nu - \frac{Q^2}{2M}\right)\tau\left|\mathcal{G}_M^V(Q^2)\right|^2,$$

$$W_{1\text{-Qelastic}}^{\nu\text{-axial}} = \delta\left(\nu - \frac{Q^2}{2M}\right)(1+\tau)\left|\mathcal{F}_A(Q^2)\right|^2,$$

$$W_{2\text{-Qelastic}}^{\nu\text{-vector}} = \delta\left(\nu - \frac{Q^2}{2M}\right)\left|\mathcal{F}_V(Q^2)\right|^2,$$

$$W_{2\text{-Qelastic}}^{\nu\text{-axial}} = \delta\left(\nu - \frac{Q^2}{2M}\right)\left|\mathcal{F}_A(Q^2)\right|^2,$$

$$W_{3\text{-Qelastic}}^{\nu} = \delta\left(\nu - \frac{Q^2}{2M}\right)\left|2\mathcal{G}_M^V(Q^2)\mathcal{F}_A(Q^2)\right|,$$

$$W_{4\text{-Qelastic}}^{\nu\text{-vector}} = \delta\left(\nu - \frac{Q^2}{2M}\right)\frac{1}{4}\left(\left|\mathcal{F}_V(Q^2)\right|^2 - \left|\mathcal{G}_M^V(Q^2)\right|^2\right),$$

$$W_{4\text{-Qelastic}}^{\nu\text{-axial}} = \delta\left(\nu - \frac{Q^2}{2M}\right) \times \frac{1}{4} \times \left[\mathcal{F}_A^2(Q^2) + \left(\frac{Q^2}{M^2} + 4\right)\left|\mathcal{F}_p(Q^2)\right|^2 - \left(\mathcal{F}_A(Q^2) + 2\mathcal{F}_P(Q^2)\right)^2\right],$$

$$W_{5\text{-Qelastic}}^{\nu\text{-vector}} = \delta\left(\nu - \frac{Q^2}{2M}\right)\frac{1}{2}\left|\mathcal{F}_V(Q^2)\right|^2,$$

$$W_{5\text{-Qelastic}}^{\nu\text{-axial}} = \delta\left(\nu - \frac{Q^2}{2M}\right)\frac{1}{2}\left|\mathcal{F}_A(Q^2)\right|^2,$$

where

$$\mathcal{G}_E^V(Q^2) = G_E^p(Q^2) - G_E^n(Q^2),$$
$$\mathcal{G}_M^V(Q^2) = G_M^p(Q^2) - G_M^n(Q^2).$$

and

$$\left|\mathcal{F}_V(Q^2)\right|^2 = \frac{[\mathcal{G}_E^V(Q^2)]^2 + \tau[\mathcal{G}_M^V(Q^2)]^2}{1+\tau}.$$

Here, $G_E^p(Q^2)$, $G_E^n(Q^2)$, $G_M^p(Q^2)$ and $G_M^n(Q^2)$ are the electric and magnetic nucleon form factors, which are measured in electron scattering experiments. Note that:

$$\sigma_T^{\text{vector}} \propto \tau\left|\mathcal{G}_M^V(Q^2)\right|^2; \qquad \sigma_T^{\text{axial}} \propto (1+\tau)\left|\mathcal{F}_A(Q^2)\right|^2,$$
$$\sigma_L^{\text{vector}} \propto \left(\mathcal{G}_E^V(Q^2)\right)^2; \qquad \sigma_L^{\text{axial}} = 0.$$

Therefore, for QE $\nu_\mu, \bar{\nu}_\mu$ scattering only $\mathcal{G}_M^V$ contributes to the transverse virtual boson absorption cross section.

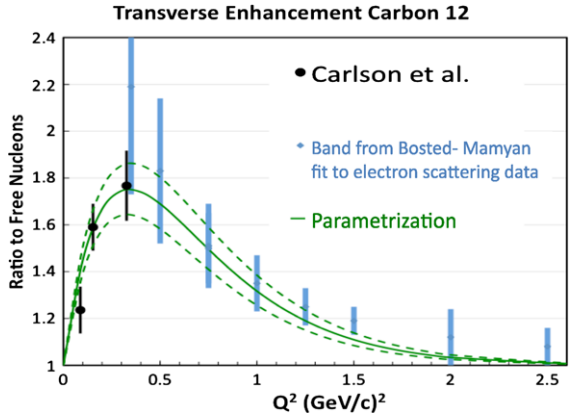

Fig. 7 The transverse enhancement ratio [20] ($\mathcal{R}_T$) as a function of Q^2. Here, $\mathcal{R}_T$ is ratio of the integrated transverse response function for QE electron scattering on nucleons bound in carbon divided by the integrated response function for independent nucleons. The *black points* are extracted from Carlson et al. [22], and the *blue bands* are extracted from a fit [25] to QE data from the JUPITER [24] experiment (Jlab experiment E04-001). The curve is a fit to the data of the form $\mathcal{R}_T = 1 + A\,Q^2 e^{-Q^2/B}$. The *dashed lines* are the upper and lower error bands (Color figure online)

4.2 Transverse enhancement QE scattering from nuclei

Studies of QE electron scattering on nuclear targets [22] indicate that only the longitudinal part of the QE cross section can be described in terms of a universal response function of independent nucleons bound in a nuclear potential (and free nucleon form factors). In contrast, a significant additional enhancement with respect to the model is observed in the transverse part of the QE cross section.

The enhancement in the transverse QE cross section has been attributed [22] to meson exchange currents (MEC) in a nucleus. Within models of meson exchange currents [22] the enhancement is primarily in the transverse part of the QE cross section, while the enhancement in the longitudinal QE cross section is small (in agreement with the electron scattering experimental data).

The conserved vector current hypothesis (CVC) implies that the corresponding vector structure function for the QE cross section in $\nu_\mu, \bar{\nu}_\mu$ scattering can be expressed in terms of the structure functions measured in electron scattering on nuclear targets. Therefore, there should also be a transverse enhancement in neutrino scattering. In models of meson exchange currents the enhancement in the axial part of $\nu_\mu, \bar{\nu}_\mu$ QE cross section on nuclear targets is also expected small.

The transverse enhancement observed in electron scattering is a function of both Q^2 and ν. However, a simple way to account for the integrated transverse enhancement [20] from nuclear effects is to assume that $G_M^p(Q^2)$ and $G_M^n(Q^2)$ are enhanced in a nuclear targets by factor $\sqrt{R_{\mathrm{TL}}}$.

Bodek, Budd and Christy [20] have used electron scattering data [22, 24, 25] to parametrize R_{TL} as follows:

$$R_{\mathrm{TL}} = 1 + A\,Q^2 e^{-Q^2/B}$$

with $A = 6.0$ and $B = 0.34$ GeV^2. The electron scattering data shown in Fig. 7 indicates that the transverse enhancement is maximal near $Q^2 = 0.3$ GeV^2 and is small for Q^2 greater than 1.5 GeV^2. The upper error band is given by $A = 6.7$ and $B = 0.35$ GeV^2, and the lower error band is given by $A = 5.3$ and $B = 0.33$ GeV^2.

In modeling $\nu_\mu, \bar{\nu}_\mu$ QE scattering on nuclear targets we use $BBBA2007_{25}$ parameterization [23] of the free nucleon electromagnetic form factors $G_E^p(Q^2)$, $G_E^n(Q^2)$, $G_M^p(Q^2)$ and $G_M^n(Q^2)$ (with $M_V^2 = 0.71\,\mathrm{GeV}^2$), and a dipole axial form factor with $M_A = 1.014$ GeV. We apply the transverse enhancement correction to $G_M^p(Q^2)$ and $G_M^n(Q^2)$. We also apply Pauli blocking corrections to the differential QE cross section as parametrized by Paschos and Yu [13]. We refer to this model as the Transverse Enhancement (TE) model. This is the nominal model that is used in this paper.

We also compare calculations based on the nominal TE model to two other models. The first model is the independent nucleon model with Pauli blocking with $M_A = 1.014$ GeV, without transverse enhancement. We refer to this model as the "Independent Nucleon (MA = 1.014)" model. This model, which is used by the NOMAD [30, 31] collaboration, is very close to the model which is currently implemented in the GENIE Monte Carlo (the GENIE default value is $M_A = 0.99$ GeV). The second model is the independent nucleon model with Pauli blocking, $M_A = 1.3$ GeV, without transverse enhancement. This model is used by the MiniBooNE Collaboration [28, 29]. We refer to this model as the "Larger M_A ($M_A = 1.3$) model". We use the difference between the three models as a conservative systematic error on the flux extracted from the ν samples.

Figure 8 shows a comparison of predictions of various model predictions for the $\nu_\mu, \bar{\nu}_\mu$ total QE cross section sections to experimental data on nuclear targets. Shown are "Independent Nucleon (MA = 1.014)" model, the "Larger M_A ($M_A = 1.3$) model", and the TE model (with upper and lower error bands). Also shown are the predictions of the "QE + np-nh RPA" MEC model of Martini et al. [26, 27]. The data points are the QE cross section measurements of MiniBooNE [28, 29] (gray stars) and NOMAD [30, 31] (purple circles). Note that there is an overall $\approx$10 % systematic error in the experimental QE cross sections because of uncertainties in the determination of the neutrino and antineutrino fluxes in each of the two experiments.

In this paper we use the error band in the transverse enhancement parameters as a lower limit on systematic error in the modeling. We use the "Independent Nucleon (MA = 1.014)" and the "Larger M_A ($M_A = 1.3$) model" as conservative upper limits on the errors in the modeling.

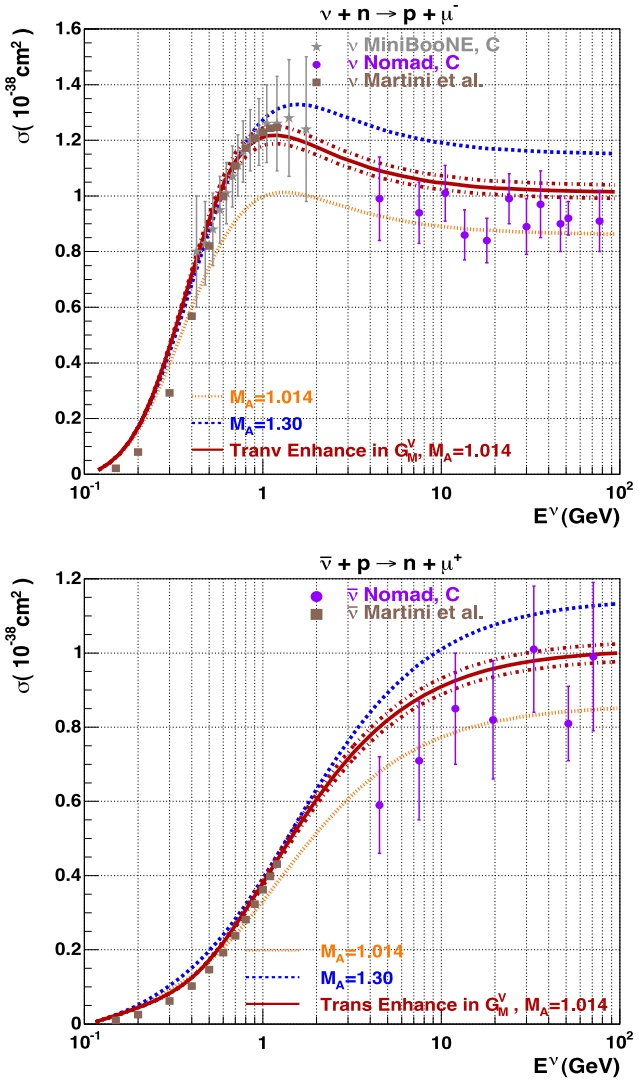

Fig. 8 Comparison of predictions for the ν_μ, $\bar{\nu}_\mu$ total QE cross section sections from the nominal TE model, the "Independent Nucleon (MA = 1.014)" model, the "Larger M_A ($M_A = 1.3$) model", and the "QE + np-nh RPA" MEC model of Martini et al. [26, 27]. The data points are the measurements of MiniBooNE [28, 29] (*gray stars*) and NOMAD [30, 31] (*purple circles*) (Color figure online)

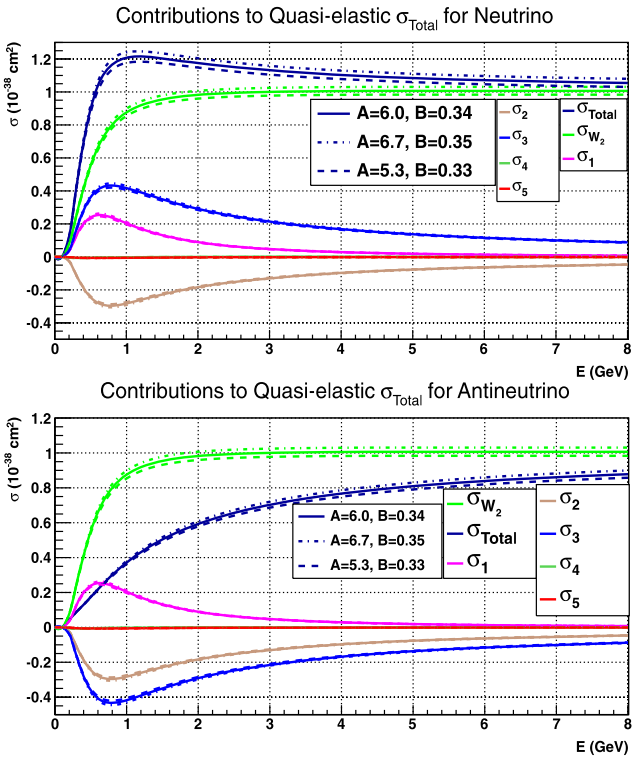

Fig. 9 Contribution of the various components (σ_{W_2}, σ_2, σ_1, σ_3, σ_4, σ_5) to the total QE cross section (as predicted by the TE model). *Top panel*: Neutrinos. *Bottom panel*: Antineutrinos (Color figure online)

Figure 9 shows the contribution of the various components (σ_{W_2}, σ_2, σ_1, σ_3, σ_4, σ_5) to the total QE cross section (as defined by Eq. (13)) as a function of incident energy. These contributions are calculated using the TE model. The top panel shows the contribution of the various components for the neutrino QE cross section, and the bottom panel shows the contribution of the various components for the antineutrino QE cross section.

4.3 Neutrino and antineutrino total cross sections

The MINOS collaboration uses the criteria that the fraction of "low-ν" events that are used for the determination of the relative neutrino flux in an energy bin should be less than 60 % of the total number of charged current events. In order to test for this fraction, we need to use a parameterization to estimate the energy dependence of the neutrino and antineutrino charged current total cross sections.

Figures 10 and 11 show the ν_μ and $\bar{\nu}_\mu$ total charged current cross sections measured on isoscalar nuclear targets by the MINOS [3] (iron), NOMAD [30, 31] (carbon), and Serpukov [32] (Serp96, aluminum) experiments. The total cross sections per nucleon (divided by neutrino energy) are shown in units of 10^{-38} cm^2/GeV (with statistical, systematic and normalization errors combined in quadrature). The ratio of the $\bar{\nu}_\mu$ and ν_μ total charged current cross sections is shown in the bottom panel of Fig. 11. The cross sections reported by the MINOS collaboration were measured using a neutrino flux extracted from "low-ν" samples with ν less than 1, 3, and 5 GeV.

Also shown in Fig. 10 are low energy cross sections measured by at BNL [33] (BNL82). Since the BNL82 cross sections were measured on a deuterium target we apply a correction to account for nuclear effects. The BNL82 points shown in the figure were increased by the difference of the predictions of the TE model for the QE cross section (which is expected to describe the cross section on a heavy nuclear target) and the "Independent Nucleon (MA = 1.014)" model (which is expected to describe the QE cross sections on deuterium).

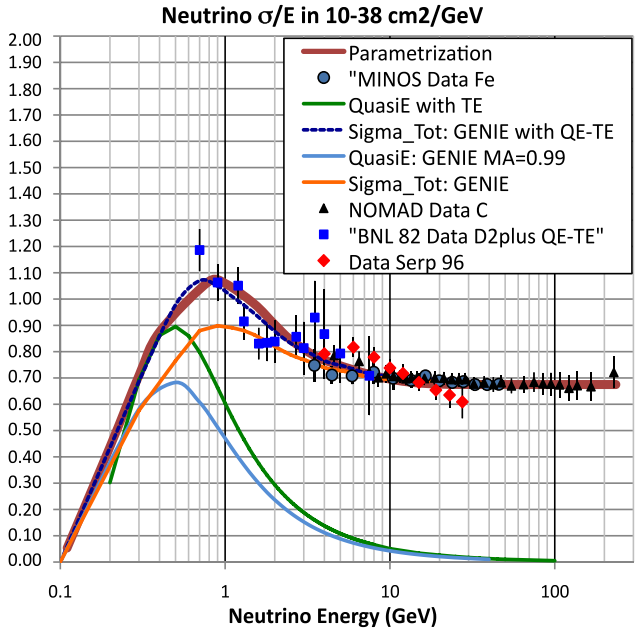

Fig. 10 The MINOS [3], NOMAD [30, 31], Serp96 [32], and BNL82 [33] (corrected) measurements of σ_{total}/E per nucleon on isoscalar nuclear targets for ν in units of 10^{-38} cm^2/GeV. The *orange line* shows the predictions of the unmodified GENIE Monte Carlo. The QE cross section in the GENIE MC is shown as the *blue line*. The QE contribution calculated with the TE model is shown as a *green line*. The *dashed blue line* shows the prediction of the modified GENIE MC (using the TE model QE cross section instead). The *thick brown line* is a parameterization described in the text (Color figure online)

The orange line shows the predictions of the GENIE Monte Carlo. The QE cross sections in the GENIE MC are computed using the independent nucleon model with $M_A = 0.99$ GeV. The QE contribution to the cross section from GENIE is shown as a blue line. The QE contribution calculated with the TE model is shown as a green line. The curve labeled GENIE with QE-TE (shown as a dotted blue line) represents the GENIE cross section increased by the difference of the predictions of the TE model for the QE cross section (which is expected to describe the cross section on a heavy nuclear target) and the "Independent Nucleon (MA = 0.99)" model (which is currently implemented in GENIE).

In our investigation of the "low-ν" technique, we use a parameterization to estimate the total ν_μ, $\bar{\nu}_\mu$ charged current cross sections. The parameterization, which is shown as the thick red line in Fig. 10, is given by

$$\frac{\sigma_\nu}{E_\nu} = \left[A + B\,e^{-E_\nu/C1} + D\,e^{-E_\nu^2/C2}\right] \times \left(1 - K e^{-(E_\nu - 0.1)/C3}\right)$$

where for ν_μ we use $A_\nu = 0.675$, $B_\nu = 0.12$, $C1_\nu = 9$ GeV, $D_\nu = 0.4$, $C2_\nu = 3$ GeV^2, $C3_\nu = 0.22$ GeV, and $K = 1.0$. For $\bar{\nu}_\mu$ we use $A_{\bar{\nu}} = 0.329$, $B_{\bar{\nu}} = -0.06$ and $C1_{\bar{\nu}} = 13$ GeV. $D_{\bar{\nu}} = 0.09$, $C2_{\bar{\nu}} = 30$ GeV^2 , $C3_\nu = 0.8$ GeV, and $K = 0.8$.

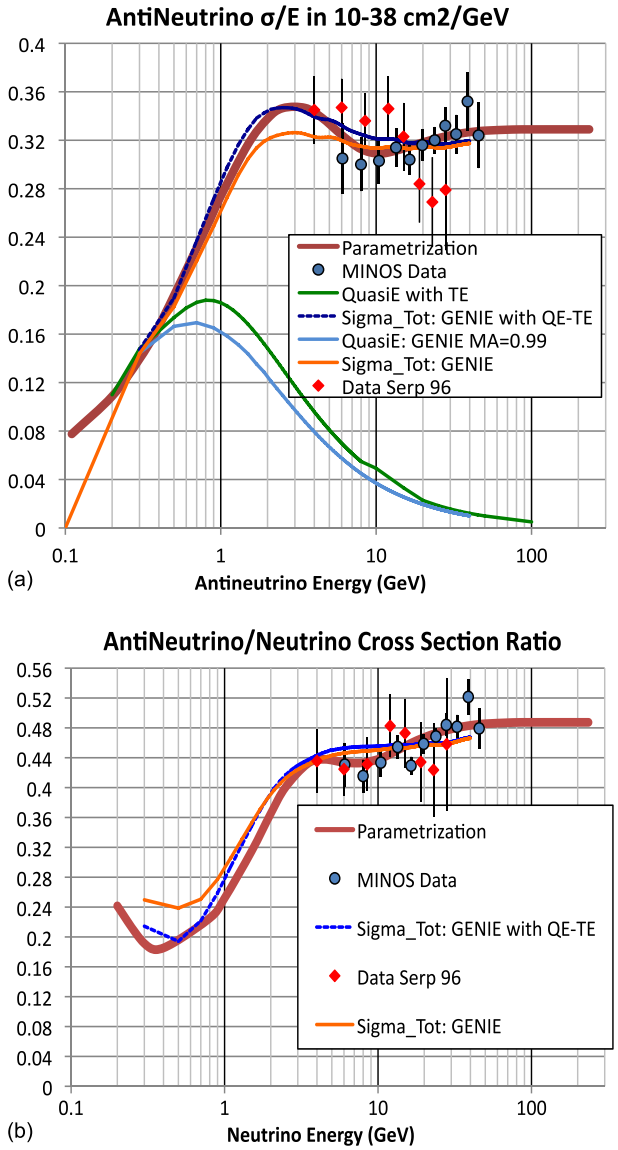

Fig. 11 Same as Fig. 10 but (**a**) for the antineutrino charged current cross section, (**b**) for the ratio of antineutrino and neutrino total cross sections (Color figure online)

Here, $\frac{\sigma_\nu}{E_\nu}$ is total charged current cross section per nucleon in units of 10^{-38} cm^2/GeV.

The above form is constrained to yield the average world cross section measurements in the 30 to 50 GeV region of 0.675×10^{-38} cm^2/GeV, and 0.329×10^{-38} cm^2/GeV for ν_μ and $\bar{\nu}_\mu$, respectively.

We only use this parameterization to estimate the fractional contribution of "low-ν" events to the total cross section to determine the region where it is less than 60 %. When improved total cross section measurements become available (e.g. from MINERvA), this parameterization can be updated to include the new data.

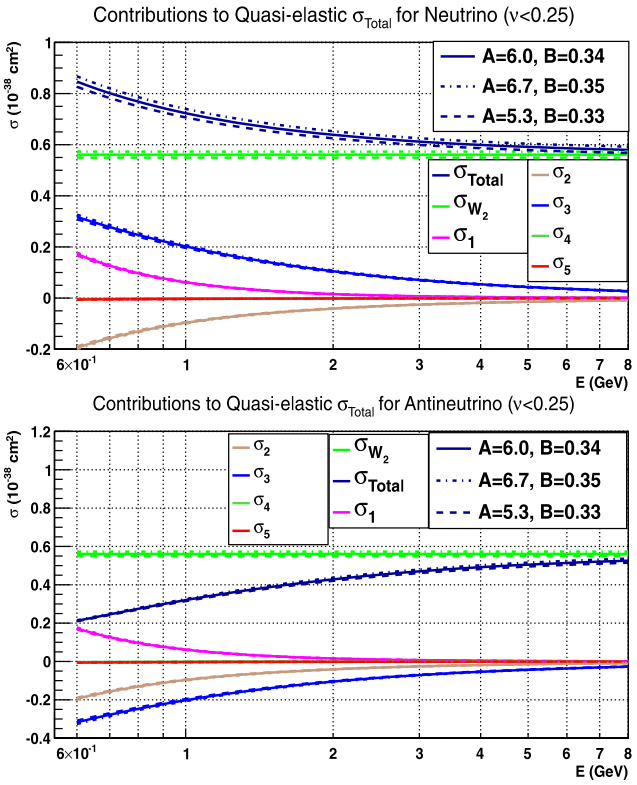

Fig. 12 Contribution of the various components (σ_{W_2}, σ_2, σ_1, σ_3, σ_4, σ_5) to the $\nu < 0.25$ GeV partial charged current cross section. This sample is dominated by QE $\nu_\mu N \to \mu^- P$ events. *Top panel*: Neutrinos. *Bottom panel*: Antineutrinos (Color figure online)

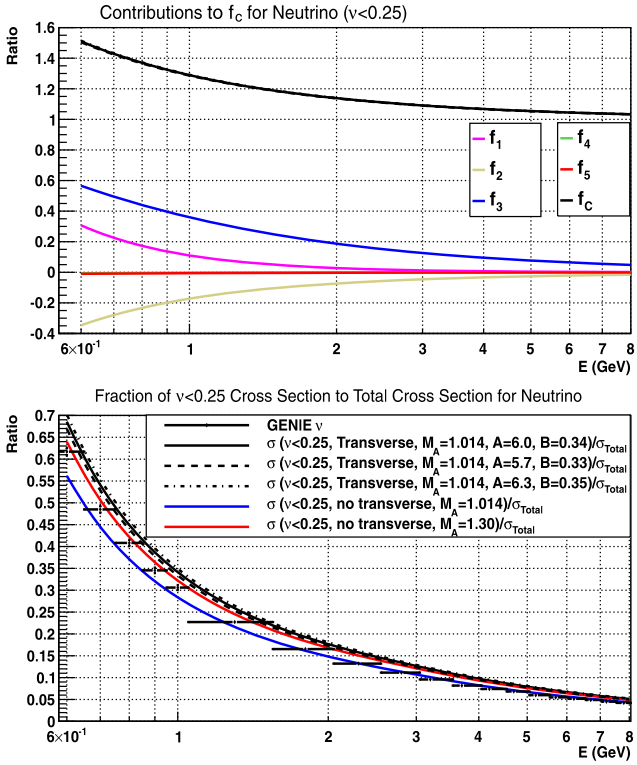

Fig. 13 The $\nu < 0.25$ GeV sample for ν_μ scattering on carbon. *Top panel*: The total correction factor f_C (*black line*), the contribution of the kinematic correction to $\mathcal{W}_2$ (f_2) (*yellow line*), the contributions from $\mathcal{W}_1$ (f_1) (*pink line*), the contribution from $\mathcal{W}_3$ (f_3) (*blue line*), and the very small contributions of $\mathcal{W}_4$ (f_4), and $\mathcal{W}_5$ (f_5). *Bottom panel*: The fractional contribution of $\nu < 0.25$ GeV events to the total ν_μ charged current cross section (Color figure online)

4.4 Results with $\nu < 0.25$ GeV

Figure 12 shows the contribution of the various components (σ_{W_2}, σ_2, σ_1, σ_3, σ_4, σ_5) to the $\nu < 0.25$ GeV partial cross section. This sample is dominated by QE $\nu_\mu N \to \mu^- P$ events. The partial cross section as a function of energy for neutrinos is shown in the top panel and the partial cross section for antineutrinos is shown in the bottom panel. The partial cross section (per nucleon) is calculated on a carbon target using the TE model.

The uncertainty in the relative values of the $\nu < 0.25$ GeV partial cross section as a function of energy determines the uncertainty in the determination of the relative fluxes. Here $f_C(E)$ is the ratio of the partial cross section to the value of the partial cross section at $E = \infty$.

Figure 13(a) (top) shows the correction factor f_C for the $\nu < 0.25$ GeV sample for neutrinos as a function energy. The error bands in f_C (originating from the uncertainty in the transverse enhancement) are shown as the dotted lines, and represent the lower limit on errors. Also shown on the figure is the negative contribution from the kinematic correction f_2 (which is well known), and the contributions of f_1, f_3, f_4 and f_5. Here the contribution of f_4 and f_5 is negligible. For the case of neutrino scattering, the positive contributions of f_1 and f_3 partially cancel the negative contribution of f_2. Figure 13(b) (bottom) shows the fractional contribution of the $\nu < 0.25$ GeV sample to the total neutrino charged current cross section. This fraction is less than 60 % for ν_μ energies above 0.70 GeV.

Figure 14 is the same as Fig. 13 for the case of antineutrinos. For the case of antineutrino scattering f_3 changes sign, and both f_2 and f_3 are negative. The fractional contribution of the $\nu < 0.25$ GeV sample to the total antineutrino charged current cross section is less than 60 % for $\bar{\nu}_\mu$ energies above 1.0 GeV.

4.4.1 *Uncertainty in the f_C correction factors*

It has been traditional to use the value and error in the effective M_A extracted from neutrino scattering data as an estimate of various uncertainties. Typically, the difference between results with $M_A = 1.014$ GeV and $M_A = 1.3$ GeV are used an upper limit on the error.

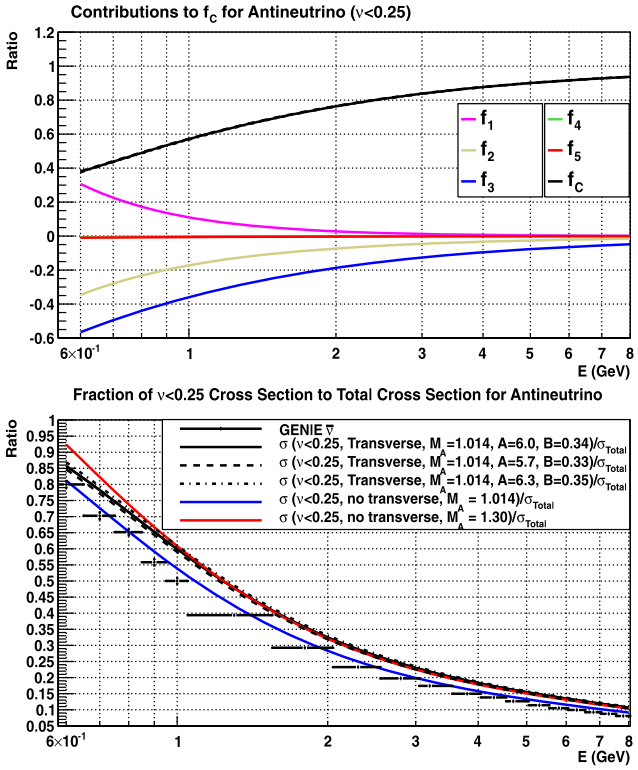

Fig. 14 Same as Fig. 13 for the case of antineutrinos

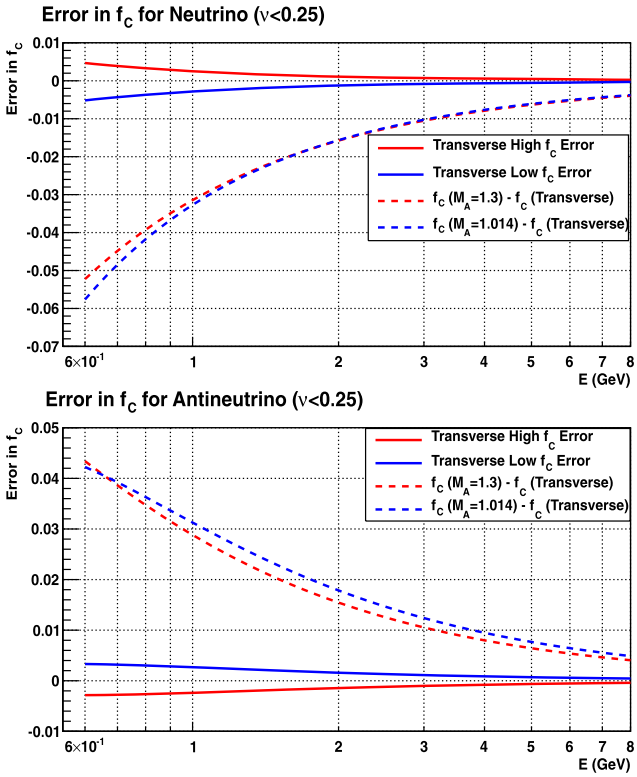

Fig. 15 The error band in the correction factor f_C for $\nu < 0.25$ GeV. *Top panel*: Neutrinos. *Bottom panel*: Antineutrinos (Color figure online)

We find that the values of the f_C correction factor are insensitive to M_A. This is because at small Q^2, both ratios f_1, and f_3 are insensitive to M_A. Specifically, both

$$\frac{\mathcal{W}_1^{\mathrm{QE}}}{\mathcal{W}_2^{\mathrm{QE}}} = \frac{(1+\tau)|\mathcal{F}_A(Q^2)|^2 + \tau|\mathcal{G}_M^V(Q^2)|^2}{|\mathcal{F}_A(Q^2)|^2 + [\mathcal{F}_V(Q^2)]^2},$$

$$\frac{\mathcal{W}_3^{\mathrm{QE}}}{\mathcal{W}_2^{\mathrm{QE}}} = \frac{|2\mathcal{G}_M^V(Q^2)\mathcal{F}_A(Q^2)|}{|\mathcal{F}_A(Q^2)|^2 + [\mathcal{F}_V(Q^2)]^2},$$

are insensitive to M_A because the change in F_A at small Q^2 is small. Since f_C is insensitive to large variations in M_A one may naively surmise that the error in f_C is small.

However, we find that the difference between the values f_C calculated with and without transverse enhancement is larger than the error estimate extracted from the uncertainty in M_A. This is because $\frac{\mathcal{W}_3^{\mathrm{QE}}}{\mathcal{W}_2^{\mathrm{QE}}}$ is sensitive to $\mathcal{G}_M^V(Q^2)$, which depends on the magnitude of the transverse enhancement at small Q^2.

Figure 15 shows the errors in f_C from the uncertainty in the TE parameters. The error originating from uncertainties in the TE parameters is also very small (less than 0.005).

We obtain a more conservative estimate of the systematic error in f_C originating from uncertainties in the modeling the QE cross section by taking the difference between f_C calculated with and without transverse enhancement. At the lowest energy of 0.7 GeV, this difference is -0.05 for ν_μ. Since at 0.7 GeV $f_C^\nu \approx 1.3$ this corresponds to a maximum error in the determination of the ν_μ flux of 3.8 %.

For $\bar{\nu}_\mu$ the difference between f_C calculated with and without transverse enhancement at an energy of 1.0 GeV is $+0.03$. Since at 1.0 GeV $f_C^{\bar{\nu}} \approx 0.6$ this corresponds a maximum error in the determination of the $\bar{\nu}_\mu$ flux of 5 %.

4.5 Comparison to GENIE and $\bar{f}_{C:\nu<0.25}(15.1\ \mathrm{GeV})$

We have used a sample of events generated by the GENIE Monte Carlo. Our studies are done at the generated level and therefore do not depend on the detector parameters or energy resolutions of any specific experiment.

We extract the energy dependence of the $\nu < 0.25$ GeV cross section from the GENIE MC sample using the following expression:

$$\sigma_{\nu<0.25}^{\mathrm{MC}}(E) = \frac{N_{\nu<0.25}^{\mathrm{MC}}(E)}{N_{\mathrm{QE}}^{\mathrm{MC}}(E)} \times \sigma_{\mathrm{QE}}^{\mathrm{MC}}(E)$$

where the superscript MC refers to events generated by the GENIE Monte Carlo.

Here, $N^{\mathrm{MC}}(E)$ is the number of events generated by the Monte Carlo with neutrino energy E, and $N_{\nu<0.25}^{\mathrm{MC}}(E)$ is the subset of these events with $\nu < 0.25$ GeV.

As mentioned earlier, we propose that the neutrino cross sections at low energy be measured relative to the neutrino

cross section at 15.1 GeV. For any cross section model we can define the normalized quantity $\bar{f}_{C:\nu<0.25}(15.1\ \text{GeV})$ as:

$$\bar{f}_{C:\nu<0.25}(15.1)(E) = \frac{\sigma_{\nu<0.25}(E)}{\sigma_{\nu<0.25}(E = 15.1\ \text{GeV})}$$

which is equivalent to

$$\bar{f}_{C:\nu<0.25}(15.1)(E) = \frac{f_{C:\nu<0.25}(E)}{f_{C:\nu<0.25}(E = 15.1\ \text{GeV})}.$$

We compare the values of $\bar{f}_{C:\nu<0.25}(15.1)(E)$ predicted by the GENIE MC to our calculations.

For completeness, we give the values of $f_{C:\nu<0.25}(15.1)$ that can be used to convert between $\bar{f}_{C:\nu<0.25}(E)$ and $f_{C:\nu<0.25}(E)$.

For the TE QE model we find $f_{C:\nu<0.25}(15.1) = 1.018$ (for ν) and 0.966 (for $\bar{\nu}$). For QE models without TE we find similar values of $f_{C:\nu<0.25}(15.1) = 1.016$ ($M_A = 1.014$) and $f_{C:\nu<0.25}(15.1) = 1.014$ ($M_A = 1.03$) for ν. For $\bar{\nu}$ we find $f_{C:\nu<0.25}(15.1) = 0.969$ for models without TE.

Comparisons of our calculated values of the normalized $\bar{f}_{C:\nu<0.25}(15.1)(E)$ to values from the GENIE MC are shown in Fig. 16. The top panel shows the comparison for neutrinos and the bottom panel shows the comparison for antineutrinos. Our calculation for the TE model is shown in black. Our calculation assuming no transverse enhancement and $M_A = 1.014$ GeV is shown in red. As mentioned earlier, the values for $M_A = 1.014$ GeV (red line) and $M_A = 1.3$ GeV (blue line) are very close to each other. The GENIE prediction (which has no transverse enhancement and uses $M_A = 0.99$ GeV) is close to the red curve as expected. The GENIE predictions include a contribution from coherent pion production. As shown in Appendix B, for the $\nu < 0.25$ GeV sample, the contribution from coherent pion production is less than 0.1 % for neutrinos and less than 0.6 % for antineutrinos.

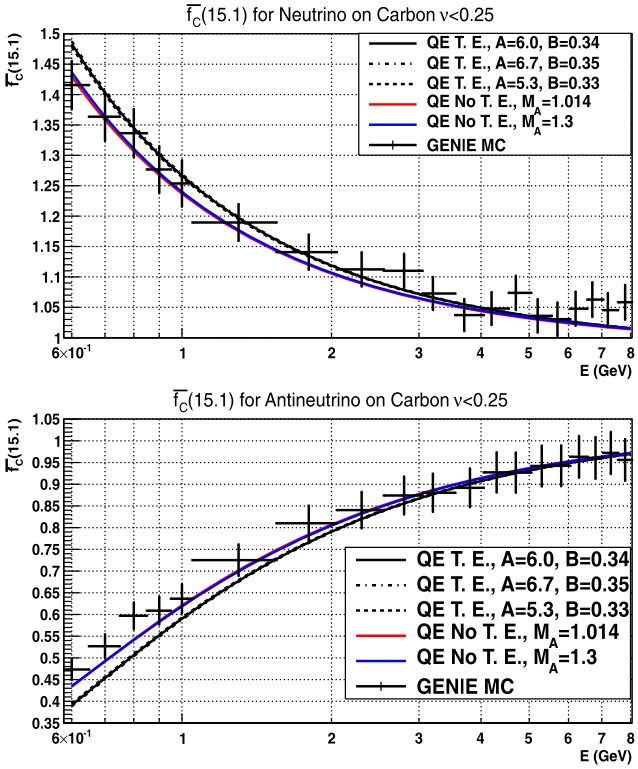

Fig. 16 Comparisons of our calculated values of the normalized $\bar{f}_{C:\nu<0.25}(15.1)(E)$ ($=\bar{f}_C(15.1)$ for $\nu < 0.25$ GeV) to values from the GENIE MC. The values calculated with the nominal TE model for QE scattering ($M_A = 1.014$ GeV) are shown in *black*. The values calculated assuming no transverse enhancement and $M_A = 1.014$ GeV are shown in *red*. The GENIE prediction (which has no transverse enhancement and uses $M_A = 0.99$ GeV) is close to the *red curve* as expected (Color figure online)

4.6 Conclusions of the studies with ν <0.25 GeV

In conclusion, we find that the method works very well for $\nu < 0.25$ GeV. If one takes the average of all the models, a conservative upper limit of the model uncertainty in the relative flux extracted from the $\nu < 0.25$ GeV sample is 1.9 % for ν_μ energies above 0.7 GeV and 2.5 % for $\bar{\nu}_\mu$ energies above 1.0 GeV. The GENIE Monte Carlo is in reasonable agreement with the models and therefore can be used to obtain a first order neutrino flux.

A study of the Q^2 distributions of QE events in MINERvA can be used to constrain the Q^2 dependence of the QE differential cross sections and thus reduce the model dependence in the determination of the relative flux to a negligible level. A GENIE Monte Carlo which is tuned to agree with the new data can be used to extend the technique to lower energies.

5 Using "low-ν" events with $\nu < 0.5$ GeV

The $\nu < 0.5$ GeV ν_μ and $\bar{\nu}_\mu$ samples have close to twice the number of events as the $\nu < 0.25$ GeV samples. These samples for scattering are also dominated by QE events, but include a significant fraction (about 1/3) of events in which a single pion is produced in the final state. As seen in Fig. 3, the $\nu < 0.5$ GeV samples are composed of QE events with $Q^2 < 0.9$ GeV^2, and $\Delta(1232)$ events with $Q^2 < 0.3$ GeV^2.

Figure 17 shows the $\nu < 0.5$ GeV partial charged current cross sections as a function of energy. The partial cross sections extracted from the GENIE Monte Carlo are shown as black points with MC statistical errors. The $\nu < 0.5$ GeV partial cross section for ν_μ scattering is shown on the top panel, and the $\nu < 0.5$ GeV partial cross section for $\bar{\nu}_\mu$ scattering is shown on the bottom panel. The QE contribution

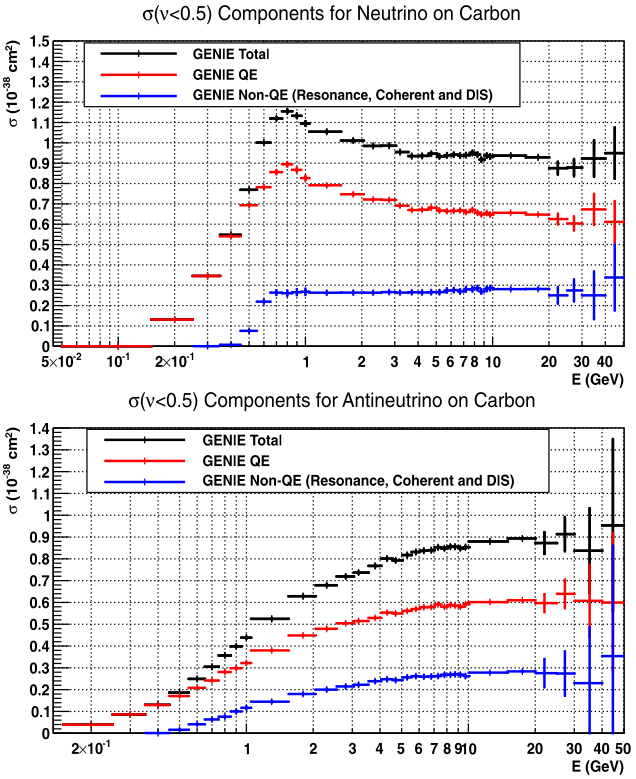

Fig. 17 The $\nu < 0.5$ GeV partial charged current cross section as a function of energy from the GENIE Monte Carlo. The QE contribution is shown in *red*, the contribution from pion production process (Δ, inelastic and coherent pion production) is shown in *blue*, and the total $\nu < 0.5$ GeV partial cross section is shown in *black*. The $\nu < 0.5$ GeV partial cross section for ν_μ is shown in the *top panel*, and the $\nu < 0.5$ GeV partial cross section for $\bar{\nu}_\mu$ is shown in the *bottom panel* (Color figure online)

to the $\nu < 0.5$ GeV partial cross section is shown in red, and the contribution from pion production processes (Δ, inelastic and coherent pion production) is shown in blue.

As seen in Fig. 17, the pion production contribution to the $\nu < 0.5$ GeV partial cross section is relatively constant with energy, while the QE contribution has some energy dependence. Therefore, the energy dependence of the sum of the two contributions to the $\nu < 0.5$ GeV partial cross section requires modeling of the relative magnitude of QE and pion production processes (specifically at low Q^2).

As shown in Figs. 18 and 19, the consistency among the experimental measurements of pion production cross sections in the region of the $\Delta(1232)$ resonance is about 20 % (depending on the neutrino energy and the nuclear target). We use this variation to get an estimate of the model uncertainty in the determination of the neutrino flux from the $\nu < 0.5$ GeV samples. This uncertainty can be greatly reduced when more precise measurements of the QE and pion production cross sections become available (e.g. from MINERvA).

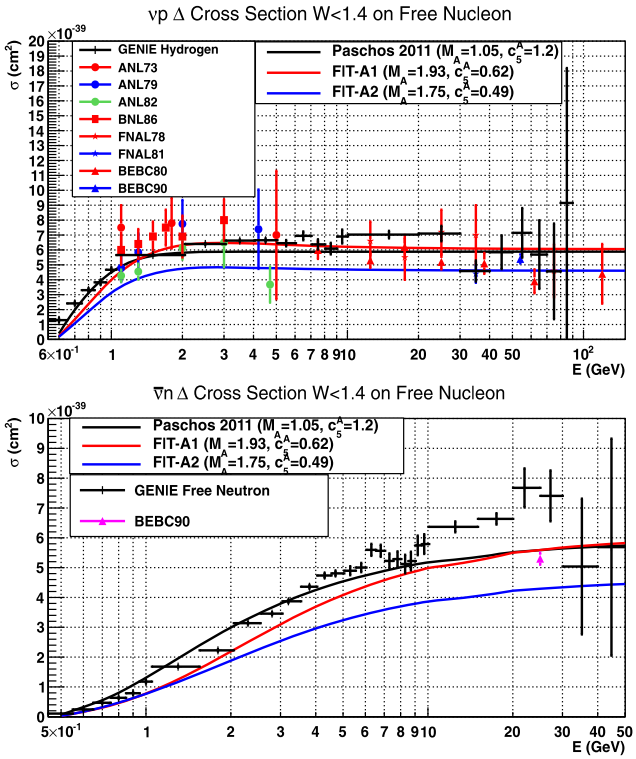

Fig. 18 $\nu_\mu P \to \mu^- \Delta^{++}$ (*top panel*) and $\bar{\nu}_\mu N \to \mu^+ \Delta^-$ (*bottom panel*) cross sections (for $W < 1.4$ GeV) measured on free nucleons (H and D), compared to predictions from the GENIE MC (*black points* with errors) (Color figure online)

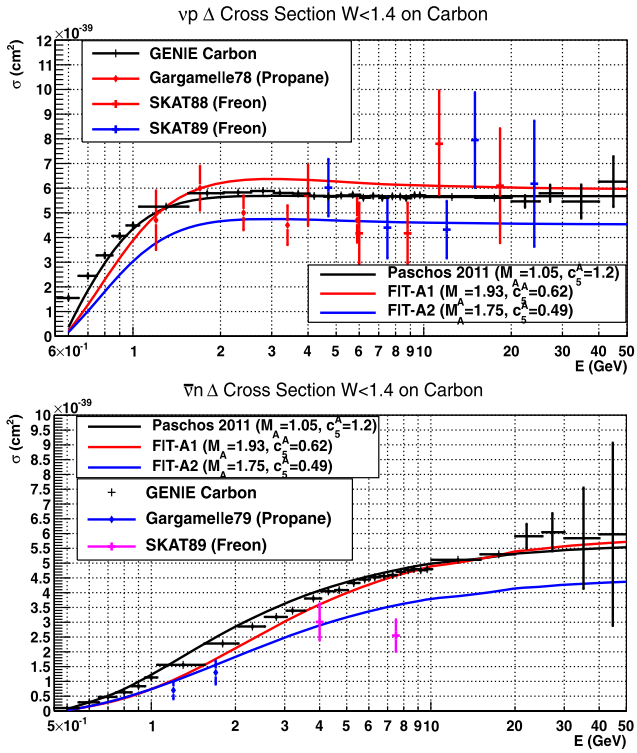

Fig. 19 Same as Fig. 18 for the case of nuclear targets (Color figure online)

6 Pion production with $W < 1.4$ GeV

In this section we describe the uncertainties in the modeling of pion production cross sections for $W < 1.4$ GeV. The antineutrino structure functions are related to the neutrino structure functions by the following relationship.

$$\mathcal{F}_i^{\bar{\nu}n} = \mathcal{F}_i^{\nu p}, \qquad \mathcal{F}_i^{\bar{\nu}p} = \mathcal{F}_i^{\nu n}. \tag{15}$$

6.1 $\nu_\mu P \to \mu^- \Delta^{++}$ and $\bar{\nu}_\mu N \to \mu^+ \Delta^-$ (FIT-A)

We define the cross section for $\nu_\mu P \to \mu^- \Delta^{++}$ as the integrated cross section for $W < 1.4$ GeV for the following single final state:

$$\nu_\mu P \to \mu^- P \pi^+.$$

We define the cross section for $\bar{\nu}_\mu N \to \mu^+ \Delta^-$ as the integrated cross section for $W < 1.4$ GeV for the following single final state:

$$\bar{\nu}_\mu N \to \mu^+ N \pi^-.$$

Therefore, our definition includes the sum of the contributions of the resonant cross section and the non-resonant continuum.

The structure functions (form factors) for the reactions $\nu_\mu P \to \mu^- \Delta^{++}$ and $\bar{\nu}_\mu N \to \mu^+ \Delta^-$ defined above are the same (except that for antineutrinos the structure function W_3 changes sign). It has been experimentally determined [43] that $\nu_\mu P$ cross section for $W < 1.4$ GeV is dominated by the resonant Δ^{++} production process. Similarly, the $W < 1.4$ GeV cross section for $\bar{\nu}_\mu N$ is dominated by the resonant Δ^- production process.

As discussed in the Appendix A, we parametrize the Δ^{++} and Δ^- production cross sections in terms of form factors as given by Paschos and Lalakulich [10–12], with the form factors of Paschos and Schalla [10–12]. In order to obtain predictions for the $W < 1.4$ GeV region, we divide all theoretical Δ production cross sections by a factor of 1.2 (because 20 % of the resonant cross section is above $W = 1.4$ GeV). We vary two of the parameters in the model, specifically M_A^Δ and C_5^A to obtain a band that span the experimental data. We extract M_A^Δ from the measured Q^2 distributions and use C_5^A to set the overall normalization.

The top panel in Fig. 18 shows a summary of cross section measurements for $\nu_\mu P \to \mu^- \Delta^{++}$ on free nucleons (hydrogen or deuterium targets.) Shown are bubble chamber measurements at low energy from Argonne (ANL73 [34], ANL79 [35], ANL82 [36]) and measurement at low energy from Brookhaven (BNL86 [37]). Also shown are measurements at higher energies from the Fermilab bubble chamber (FNAL78 [38, 39], FNAL81 [40]) and high energy data from CERN (BEBC80 [41, 42], BEBC80 [43]). The bottom panel in Fig. 18 shows the BEBC90 [43] cross section measurements for $\bar{\nu}_\mu N \to \mu^+ \Delta^-$ on free nucleons (deuterium target). The predictions from the GENIE MC on free nucleons (shown as black points with MC statistical errors) are near the upper bound of our three parameterizations.

The black curve labeled Paschos-2011 ($M_A^\Delta = 1.05$, $C_5^A = 1.2$) uses the original values of M_A^Δ and C_5^A from the paper [10–12] by Paschos and Lalakulich. These values were obtained from fits to cross sections and Q^2 distributions measured at low energies at Brookhaven and Argonne. The red curve labeled FIT-A1 ($M_A^\Delta = 1.93$, $C_5^A = 0.62$) is derived from a fit to the cross sections and Q^2 distribution of the higher energy BEBC90 [43] data for $\bar{\nu}_\mu N \to \mu^+ \Delta^-$. The blue curve labeled FIT-A2 ($M_A^\Delta = 1.75$, $C_5^A = 0.49$) is derived from a fit to the cross sections and Q^2 distribution of the higher energy BEBC90 [43] data for $\nu_\mu P \to \mu^- \Delta^{++}$.

The top panel in Fig. 19 shows a summary of cross section measurements for $\nu_\mu P \to \mu^- \Delta^{++}$ data on nuclear targets. Shown are the measurements of Gargamelle78 [44] (Propane), SKAT88 [45] (Freon), and SKAT89 [46] (Freon). The bottom panel shows measurements of $\bar{\nu}_\mu N \to \mu^+ \Delta^-$ cross sections on nuclear targets from Gargamelle78 [47] (Propane) and SKAT89 [46] (Freon).

Aside from Pauli suppression and final state interaction, the structure functions (form factors) for the processes in Figs. 18 and 19 are the same. The black (Paschos-2011), red (FIT-A1) and blue (FIT-A2) curves shown in Figs. 18 and 19 use the free nucleon form factors (but include the Pauli suppression for the case of nuclear targets). The calculations do not include the effect of final state interaction for the nuclear targets. The three curves (Paschos-2011, FIT-A1 and FIT-A2) conservatively span all the available Δ^{++} and Δ^- production cross sections on hydrogen, deuterium and nuclear targets, as shown in Figs. 18 and 19. The cross sections for the production of Δ^{++} and Δ^- on nuclear targets predicted by GENIE are near the upper bound of our three parameterizations. Additional details are given in the Appendix A.

6.2 $\nu_\mu N \to \mu^- \Delta^+$ and $\bar{\nu}_\mu P \to \mu^+ \Delta^0$ (FIT-B)

We define the cross section for $\nu_\mu N \to \mu^- \Delta^+$ as the sum of the integrated cross sections for $W < 1.4$ GeV for the following two final states:

$$\nu_\mu P \to \mu^- N \pi^+,$$
$$\nu_\mu P \to \mu^- P \pi^0.$$

We define the cross section for $\bar{\nu}_\mu P \to \mu^+ \Delta^0$ as the sum of the integrated cross sections for $W < 1.4$ GeV for the following two final states:

$$\bar{\nu}_\mu N \to \mu^+ P \pi^-,$$
$$\bar{\nu}_\mu N \to \mu^+ N \pi^0.$$

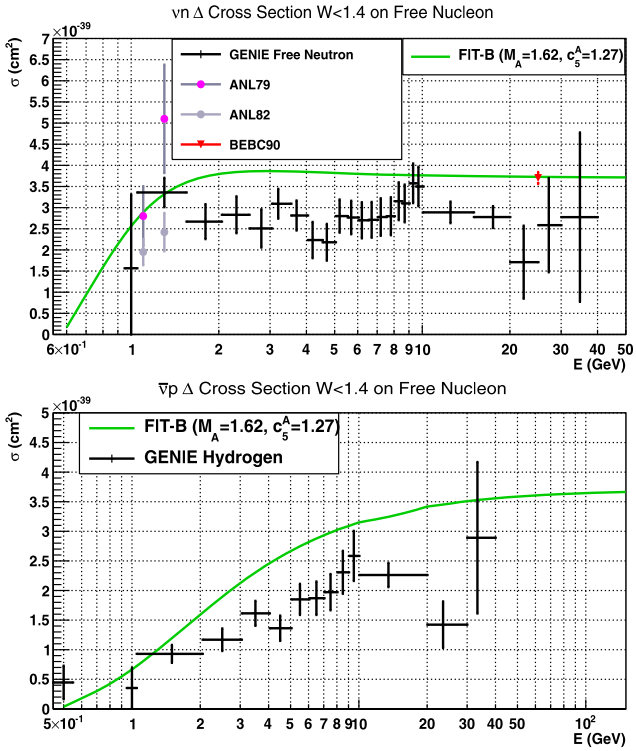

Fig. 20 $\nu_\mu N \to \mu^- \Delta^+$ (*top panel*) and $\bar{\nu}_\mu P \to \mu^+ \Delta^0$ (*bottom panel*) cross sections ($W < 1.4$ GeV) measured on free nucleons (H or D). The predictions from the GENIE MC are shown as black points with errors (Color figure online)

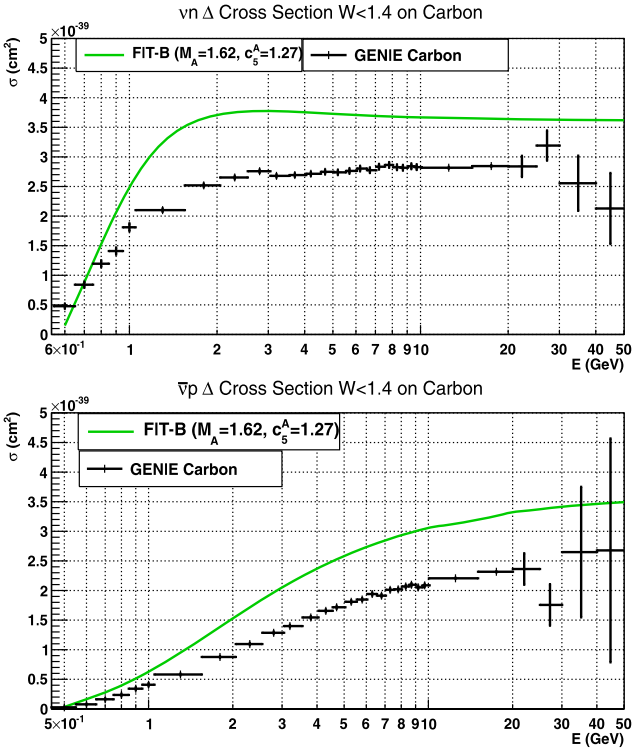

Fig. 21 Same as Fig. 20 for nuclear targets (Color figure online)

Therefore, our definition includes the sum of the contributions of the resonant cross section and non-resonant continuum.

The structure functions (form factors) for the reactions $\nu_\mu N \to \mu^- \Delta^+$ and $\bar{\nu}_\mu P \to \mu^+ \Delta^0$ defined above are the same (except that for antineutrinos the structure function W_3 changes sign). Because of Clebsch-Gordan coefficients [10–12] the resonant cross section for Δ^+ production in $\nu_\mu N$ collisions is a third of the resonant cross section for Δ^{++} production in $\nu_\mu P$ collisions. Similarly, the resonant cross section for Δ^0 production in $\bar{\nu}_\mu P$ collisions is a third of the cross section for resonant production of Δ^- in $\bar{\nu}_\mu N$ collisions.

However, unlike the case for $\nu_\mu P$ (Δ^{++}) and $\bar{\nu}_\mu N$ (Δ^-), where the cross sections are dominated by the resonant process, there is a significant contribution from the non-resonant continuum to the $W < 1.4$ GeV cross section in $\nu_\mu N$ and $\bar{\nu}_\mu P$ collisions.

The top panel of Fig. 20 shows the $\nu_\mu N \to \mu^- \Delta^+$ cross sections ($W < 1.4$ GeV) measured on free nucleons (deuterium). Shown are measurements from ANL79 [35], ANL82 [36], and BEBC90 [43]. The predictions from the GENIE MC are shown as black points with MC statistical errors. In order to describe the data (which has a large non-resonant contribution) we changed the parameters in the Paschos and Lalakulich [10–12] resonance model to fit the observed Q^2 distribution and total $W < 1.4$ GeV cross sections. The green curve labeled FIT-B ($M_A^\Delta = 1.62$, $C_5^A = 1.27$) is derived from a fit to the $W < 1.4$ GeV cross sections and Q^2 distribution of the BEBC90 [43] data for $\nu_\mu N \to \mu^- \Delta^+$. This curve provides a parameterization which describe the experimental data for the production of Δ^+ (with neutrinos) and Δ^0 (for antineutrinos) on free nucleons. The GENIE MC cross sections for the production of Δ^+ on free nucleons are lower than the fit.

The structure functions (form factors) for the reactions $\nu_\mu N \to \mu^- \Delta^+$ and $\bar{\nu}_\mu P \to \mu^+ \Delta^0$ ($W < 1.4$ GeV) are same. The bottom panel of Fig. 20 shows a comparison of the predictions of FIT-B ($M_A^\Delta = 1.62$, $C_5^A = 1.27$) (green curve) for the $\bar{\nu}_\mu P \to \mu^+ \Delta^0$ cross sections on free nucleons compared to the predictions from the GENIE MC which are shown as black points with MC statistical errors. The GENIE MC cross sections for the production of Δ^0 on free nucleons are lower than the fit.

Figure 21 shows the prediction of FIT-B ($M_A^\Delta = 1.62$, $C_5^A = 1.27$) (green curve) for the $\nu_\mu N \to \mu^- \Delta^+$ (top panel) and $\bar{\nu}_\mu P \to \mu^+ \Delta^0$ (bottom panel) $W < 1.4$ GeV cross sections on nuclear targets compared to predictions from the GENIE MC (black points with MC statistical errors). The cross sections on nuclear targets are expected to be somewhat lower than the cross sections on free nucleons shown in Fig. 20. Here, FIT-B includes the effect of Pauli suppression (but not final state interaction). The GENIE MC cross

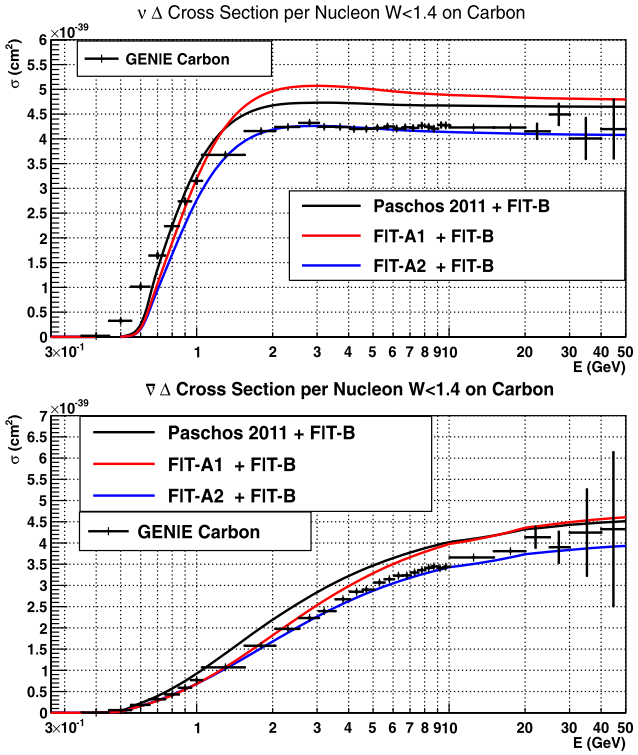

Fig. 22 The total cross sections on carbon (per nucleon) predicted by GENIE for $W < 1.4$ GeV (black points with MC statistical errors) for $\nu_\mu C \to (\mu^- \Delta^{++}$ or $\Delta^+)$ are shown on the *top panel*, and for $\bar{\nu}_\mu C \to \mu^+ (\Delta^0$ or $\Delta^-)$ are shown on the *bottom panel* (Color figure online)

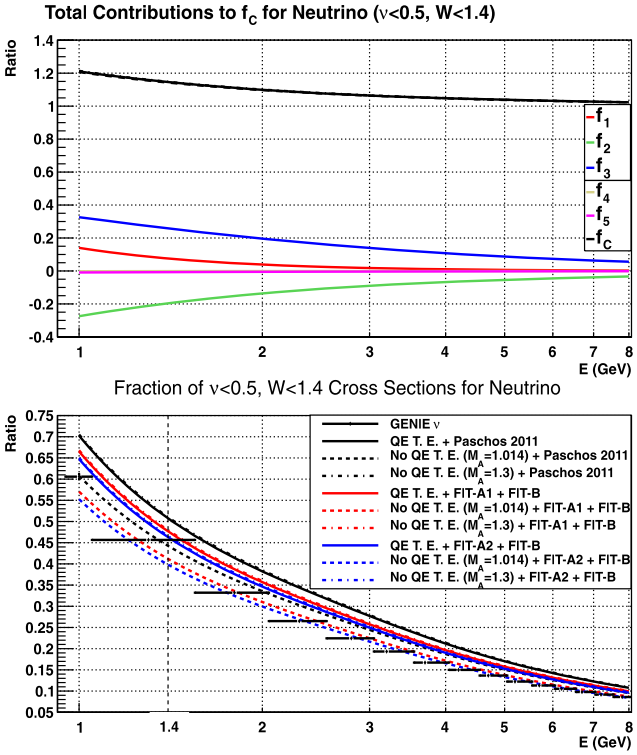

Fig. 23 The $\nu < 0.5$ GeV sample for ν_μ. This sample includes both QE $\nu_\mu N \to \mu^- P$ events (≈66 %) and Δ production events (≈33 %). *Top panel*: The total corrections factor f_C (with error bands) and the contributions of the kinematic correction to $\mathcal{W}_2$ (f_2), and the contributions from $\mathcal{W}_1$ (f_1), $\mathcal{W}_3$ (f_3), $\mathcal{W}_4$ (f_4), and $\mathcal{W}_5$ (f_5). *Bottom panel*: The fractional contribution of $\nu < 0.5$ GeV events to the total cross section (Color figure online)

sections for the production of Δ^+ and Δ^0 on nuclear targets are lower than the fit. Additional details are given in the Appendix A.

6.3 Comparisons of $W < 1.4$ GeV cross sections on carbon

A more relevant comparison is to determine how well the GENIE Monte Carlo describes the sum of the proton and neutron cross sections on carbon, since it is the total number of $\nu < 0.5$ GeV events on carbon that are used in the determination of the neutrino flux.

Figure 22 shows the predictions from the GENIE MC for total Δ production cross section for $W < 1.4$ GeV on carbon (per nucleon). The neutrino cross sections for $\nu_\mu C \to \mu^- (\Delta^{++}$ or $\Delta^+)$ are shown in the top panel, and the antineutrino cross sections $\bar{\nu}_\mu C \to (\mu^+ \Delta^0$ or $\Delta^-)$ are shown in the bottom panel. The cross sections which are predicted by GENIE are compared to our three parameterizations. (Paschos-2011, FIT-A1 and FIT-A2 for Δ^{++} and Δ^-, and FIT-B for Δ^+ and Δ^0.) The GENIE cross section predictions for the total Δ production cross sections on carbon (which use the Rein and Seghal model [48, 49] for resonance production) fall near the lower bound of our three parameterizations of the experimental data.

As described below, the uncertainties in the measurements of the Δ production cross sections do not place a serious limitation on the flux extractions using the low ν method.

6.4 Determination of neutrino and antineutrino flux using $\nu < 0.5$ GeV samples on carbon

The $\nu < 0.5$ GeV sample includes both QE $\nu_\mu N \to \mu^- P$ events (≈66 %) and Δ production events (≈33 %).

The top panel of Fig. 23 shows the total correction factor $f_C(E)$ for the $\nu < 0.5$ GeV sample (defined as $f_{C:\nu<0.5}(E)$) for *neutrino* running. Also shown are the various contributions to $f_{C:\nu<0.5}(E)$ including the kinematic correction to $\mathcal{W}_2$ (f_2), and the contributions from $\mathcal{W}_1$ (f_1), $\mathcal{W}_3$ (f_3), $\mathcal{W}_4$ (f_4), and $\mathcal{W}_5$ (f_5). The bottom panel shows the fractional contribution of $\nu < 0.5$ GeV events to the charged current neutrino total cross section. Using our nominal model (TE model for QE scattering and the Paschos 2011 model for Δ production) we find that the fraction of $\nu < 0.5$ GeV events is less than 60 % for ν_μ energies above 1.2 GeV.

The top panel of Fig. 24 shows the total correction factor $f_{C:\nu<0.5}(E)$ for *antineutrino* running. Also shown are

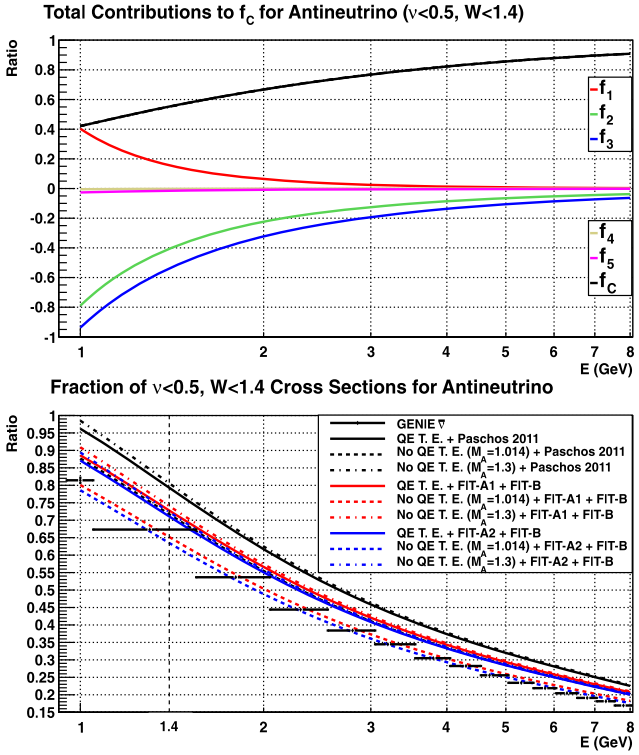

Fig. 24 Same as Fig. 23 for the case of antineutrinos (Color figure online)

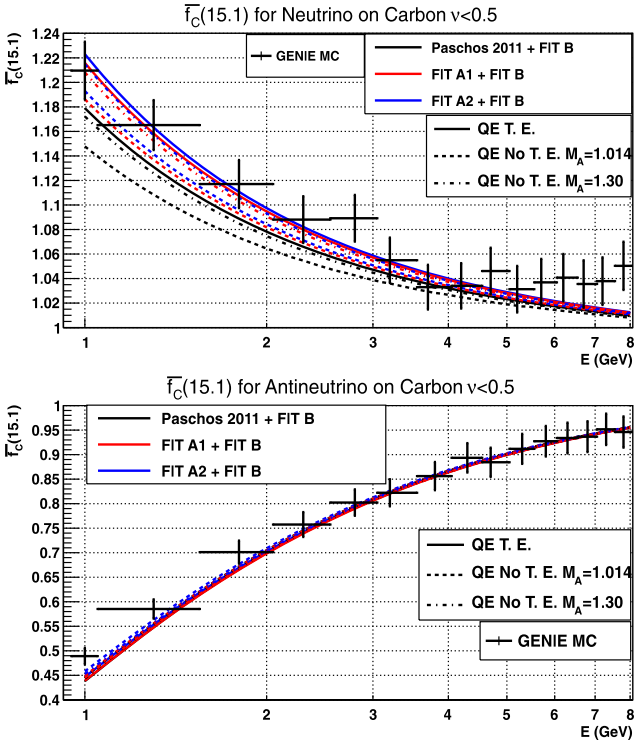

Fig. 25 Comparisons of our calculated values of the normalized $\bar{f}_{C:\nu<0.5}(15.1)(E)$ $(=\bar{f}_C(15.1)$ for $\nu < 0.5$ GeV) to values from the GENIE MC. Our nominal model (shown as the *solid black line*) uses the TE model for QE scattering and the Paschos 2011 model for Δ production. Neutrinos are shown on the *top panel* and antineutrinos are shown on the *bottom panel* (Color figure online)

the various contributions to $f_{C:\nu<0.5}$ including the kinematic correction to $\mathcal{W}_2$ (f_2), and the contributions from $\mathcal{W}_1$ (f_1), $\mathcal{W}_3$ (f_3), $\mathcal{W}_4$ (f_4), and $\mathcal{W}_5$ (f_5). The bottom panel shows the fractional contribution of $\nu < 0.5$ GeV events to the charged current antineutrino total cross section. Using our nominal model (TE model for QE scattering and the Paschos 2011 model for Δ production) we find that the fraction of $\nu < 0.5$ GeV events is less than 60 % for $\bar{\nu}_\mu$ energies above 2 GeV.

As for the $\nu < 0.25$ sample, we propose that the neutrino and antineutrino cross sections at low energy be measured relative to the cross sections at 15.1 GeV. Therefore, we define normalized quantity $\bar{f}_{C:\nu<0.5}(15.1)(E)$ for the $\nu < 0.5$ sample as:

$$\bar{f}_{C:\nu<0.5}(15.1)(E) = \sigma_{\nu<0.5}(E)/\sigma_{\nu<0.5}(E = 15.1\ \text{GeV})$$

which is equivalent to

$$\bar{f}_{C:\nu<0.5}(15.1)(E) = f_C(E)/f_C(E = 15.1\ \text{GeV}).$$

Here, $f_{C:\nu<0.5}(E = 15.1\ \text{GeV}) = 1.0113$ (for ν) and 0.9507 (for $\bar{\nu}$). These values can be used to convert between $\bar{f}_{C:\nu<0.5}(E)$ and $f_{C:\nu<0.5}(E)$.

Figure 25 shows comparisons of our calculated values of the normalized $\bar{f}_{C:\nu<0.5}(15.1)(E)$ (shown as the solid black line) to values extracted from the GENIE MC. The GENIE predictions include a contribution from coherent pion production. As shown in Appendix B, for the $\nu < 0.50$ GeV sample, the contribution from coherent pion production is less than 0.7 % for neutrinos and less than 3 % for antineutrino.

Our values are calculated from our nominal model which uses the TE model for QE scattering and the Paschos 2011 model for Δ production. Neutrinos are shown on the top panel and antineutrinos are shown on the bottom panel (color online).

Figure 26 shows the error band in the correction factor $\bar{f}_{C:\nu<0.5}(15.1)(E)$ for neutrinos (top panel) and antineutrinos (bottom panel). The error band are defined as the differences between our nominal model and other model assumptions. For neutrinos with energies greater than 1.2 GeV, the error in $\bar{f}_C(15.1)$ is less than 0.03, which corresponds to a 2.6 % upper limit on the model uncertainty in the neutrino flux extracted from the $\nu < 0.5$ GeV sample. For antineutrinos with energies greater than 2 GeV the error in $\bar{f}_C(15.1)$ is less than 0.01 (which corresponds to a 1.4 % upper limit on the model uncertainty in the antineutrino flux extracted from the $\nu < 0.5$ GeV sample).

In order to go to lower neutrino and antineutrino energies we need to use the $\nu < 0.25$ GeV sample. The model uncertainty in the relative flux extracted from the $\nu < 0.25$ GeV

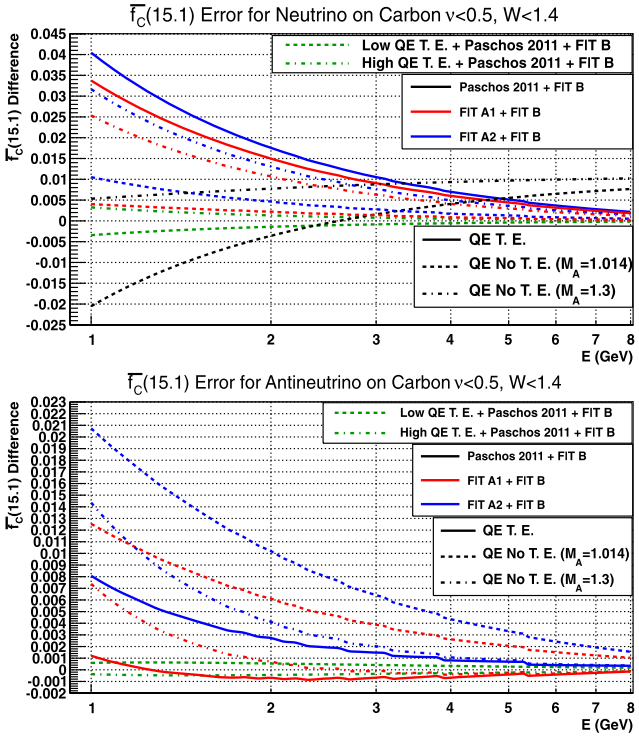

Fig. 26 The error band in the normalized correction factor $\bar{f}_{C:\nu<0.5}(15.1)(E)$ ($=\bar{f}_C(15.1)$ for $\nu < 0.5$ GeV). Our nominal model is QE with transverse enhancement and the Paschos 2011 model for Δ production. Shown are the differences between our nominal model and other model assumptions for neutrinos (*top panel*) and for antineutrinos (*bottom panel*) (Color figure online)

sample is 1.9 % for ν_μ energies above 0.7 GeV and 2.5 % for $\bar{\nu}_\mu$ energies above 1.0 GeV. With improved determination of QE and Δ production cross sections (e.g. in MINERvA), the model uncertainties can be further reduced, and the method may be extended to lower energies.

6.5 Resolution, acceptance and radiative corrections

The $\nu < 0.25$ GeV events are primarily QE events with $Q^2 < 2M \times 0.25 \approx 0.45$ GeV^2. We can select either all events with $\nu < 0.25$ GeV or only QE events with $Q^2 < 0.5$ GeV^2.

The ratio of the number of reconstructed events with $\nu < 0.25$ GeV (or $Q^2 < 0.5$ GeV^2) in data and MC as a function of energy is proportional to the ratio of the true flux to the simulated flux in the MC. This ratio provides a measure of the relative neutrino flux as a function of energy. A complete Monte Carlo should include the small contributions from coherent pion production (shown in Appendix B), strange particle production such as QE production of hyperons [50, 51], and radiative corrections [52–57]. The effects of experimental resolution and acceptance should also be simulated.

At present the GENIE Monte Carlo includes coherent pion production, but does not include the QE production of hyperons, nor radiative effects.

If the GENIE Monte Carlo is used, then one may wish to weight the rate of QE events (as a function of Q^2) by the ratio of events expected in the TE model to the number of events predicted by the model which is implemented in GENIE (i.e. the "Independent Nucleon" model with $M_A = 0.99$ GeV). In addition, QE production of hyperons and radiative effects need to be added.

7 Conclusions

We find that the model uncertainties in using the "low-ν" event samples with $\nu < 0.25$ and $\nu < 0.5$ GeV are well under control (less than 3 %). Therefore, the "low-ν" technique can be used at low energies (0.7 GeV for neutrinos and 1 GeV for antineutrinos). Once data from MINERvA on QE scattering and resonance production becomes available, the model uncertainties can be made even smaller, and the technique may be extended to even lower energies.

Since the model uncertainties are under control, the dominant systematic error originates from how well the detector response is understood, Specifically, the mis- reconstruction of high ν events as "low-ν" events must be modeled reliably. This is because at high energies (as shown in Fig. 2) mis-reconstruction of the hadron energy of high ν events can increase the number of "low-ν" events, while at low energies there are fewer high ν events that can be mis-reconstructed at low ν.

The dominant uncertainty in the method comes from the calibration and resolution smearing in the measurement of the hadronic energy. This was the dominant error when this method was used in MINOS because of the poor resolution of the MINOS target calorimeter at low hadronic energy.

As mentioned in the introduction, the standard method for the determination of the neutrino flux requires the modeling of pion production as well as the complicated magnetic focusing elements. The determination of the flux for the Fermilab NUMI beam with the standard method is limited at present by the uncertainties in pion production cross sections. The resulting error in the flux is about 5 % at low energies (1–2 GeV) and 10 %–15 % at the higher energies (10–20 GeV). Therefore, having the "low ν" method which yields the relative neutrino flux as a function of energy very useful. In principle, the uncertainties in the standard method can be improved with better measurements of pion and kaon production cross sections. Plans for such future measurements at the CERN Laboratory are currently under discussion.

A second method, which requires the measurement of the muon rate downstream of the decay pipe, can not determine

the energy dependence of the flux. It mostly constrains the overall level of the flux. At present, the uncertainties in the overall calibration of the muon chambers yields an uncertainty in the flux of about 10 %.

A third method uses inverse muon decay $\nu_\mu + e \to \mu^- + \nu_e$ events in the detector. The threshold for this reaction is about 12 GeV. Therefore, this method can only be used at higher energies. Inverse muon decay was used by NOMAD to constrain their neutrino flux at high energies. In addition to being statistically limited, the final state energy of inverse muon decay events is not fully measured since there is a neutrino in the final state. This places a limitation on the determination of the energy dependence of the neutrino fluxes. This method cannot be used for the determination of the flux for antineutrinos.

A fourth method uses the neutral current reaction $\nu_\mu + e \to \nu_\mu + e$. In addition to being statistically limited, the final state energy in $\nu_\mu + e \to \nu_\mu + e$ events is not fully measured since there is a neutrino in the final state. This places a limitation on the determination of the energy dependence of the fluxes. In this method only the sum of the fluxes for neutrinos and antineutrinos is measured because calorimetric detectors such as MINERvA cannot determine the charge of final state electrons.

Appendix A: Δ production cross sections

A.1 Δ production form factors

For the vector contribution we use the formulae for the structure functions $\mathcal{W}_1$, $\mathcal{W}_2$, $\mathcal{W}_3$, $\mathcal{W}_4$, and $\mathcal{W}_5$ on free nucleons from Lalakulich and Paschos [10–12]. We neglect the effect of Fermi motion. The form factors that we use are taken from Paschos and Schalla [10–12]. Specifically, the vector form factors are

$$C_3^V(Q^2) = \frac{2.13/D_V}{1+\frac{Q^2}{4M_V^2}}, \qquad C_4^V(Q^2) = \frac{-1.51/D_V}{1+\frac{Q^2}{4M_V^2}}, \quad \text{(A.1)}$$

$$C_5^V(Q^2) = \frac{0.48/D_V}{1+\frac{Q^2}{0.776M_V^2}} \quad \text{and} \quad D_V = \left(1+\frac{Q^2}{M_V^2}\right)^2 \quad \text{(A.2)}$$

with $M_V = 0.84$ GeV, which have been extracted from electroproduction data.

For the vector-axial interference $W_3(Q^2, \nu)$ Paschos and Schalla use the form factor $C_5^A(Q^2)$ where

$$C_5^A(Q^2) = \frac{C_5^A}{(1+Q^2/M_A^2)^2}\frac{1}{1+2Q^2/M_A^2},$$

$$C_4^A = -\frac{1}{4}C_5^A(Q^2).$$

Here, we define $C_5^A = C_5^A(0)$.

Paschos and Schalla use low energy $\pi^+ p \to \Delta^{++}$ where the non-resonant background is smallest. With $M_A = 1.05$ GeV they extract value of $C_5^A(0) = 1.08$ from the data. Since this value is close to 1.20 predicted by the Goldberger-Treiman relation, they chose to use $C_5^A = 1.2$.

Paschos and Schalla mention that several recent articles also calculate $C_5^A(0)$ by fitting experimental data [58–64] with values varying from 0.87 up to 1.20. Models with a resonant background [58, 59] prefer the power value, while the other articles [60–64] prefer values closer to 1.20. The reasons for the differences is the treatment of the non-resonant background, the form of the axial form factor that is used, and the exact kinematics at small Q^2.

For Δ^{++} and Δ^- we define the Pachos-2011 parameterization using above form factors with $C_5^A = 1.2$ (extracted through PCAC), $M_A = 1.05$ GeV, and the vector form factors described above. As mentioned earlier, FIT-A1 and FIT-A2 use the same form but with different values of C_5^A and M_A.

For Δ^+ and Δ^0 production our Fit-B uses the same form factors multiplied by a factor of $1/\sqrt{(3)}$ (as expected from Clebsch-Gordan coefficients [10–12]). However, in order to account for the large non-resonance background, we use different values C_5^A and M_A.

A.2 Various parameterizations

The low energy and high energy data for neutrino and antineutrino production of the $\Delta(1232)$ resonance are not entirely consistent. Therefore, we use range of parameterization to span the systematic error in our modeling of Δ production cross sections.

The form factors for $\nu_\mu P \to \mu^- \Delta^{++}$ and $\bar{\nu}_\mu N \to \mu^+ \Delta^-$ should be the same. The $d\sigma/dQ^2$ differential cross sections ($W < 1.4$ GeV) for $\nu_\mu P \to \mu^- \Delta^{++}$ measured at high energies are shown in the top panel of Fig. 27 (Allasia et al., BEBC90 [43] data on deuterium) and also on the top panel of Fig. 28 (Allen et al. BEBC80 [41, 42] data on hydrogen). The bottom panel of Fig. 27 shows the $d\sigma/dQ^2$ cross sections at high energies ($W < 1.4$ GeV) for $\bar{\nu}_\mu N \to \mu^+ \Delta^-$ measured by Allasia et al. (BEBC90) data on deuterium. The black curve labeled Paschos-2011 ($M_A^\Delta = 1.05$, $C_5^A = 1.2$) is from fits to lower energy $\nu_\mu P \to \mu^- \Delta^{++}$ data (BNL and Argonne). The red curve labeled FIT-A1 ($M_A = 1.93$, $C_5^A = 0.62$) is a fit to the BEBC90 $\bar{\nu}_\mu N \to \mu^+ \Delta^-$ data. The blue curve labeled FIT-A2 ($M_A = 1.75$, $C_5^A = 0.49$) is a fit to the BEBC90 $\nu_\mu P \to \mu^- \Delta^{++}$

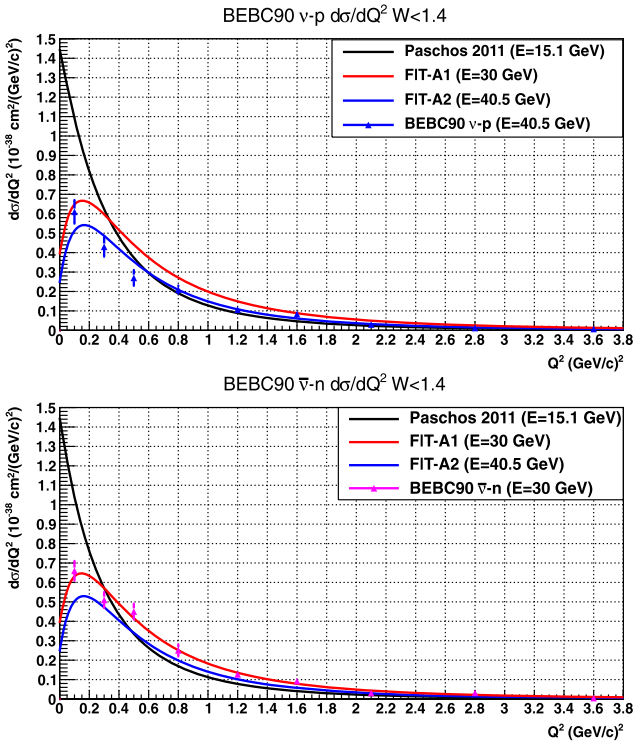

Fig. 27 $d\sigma/dQ^2$ cross sections (for $W < 1.4$ GeV) measured on deuterium at high energies by Allasia et al. (BEBC90 [43]). The cross sections for $\nu_\mu P \to \mu^- \Delta^{++}$ are shown on the *top panel* and the cross sections for $\bar{\nu}_\mu N \to \mu^+ \Delta^-$ are shown on the *bottom panel* (Color figure online)

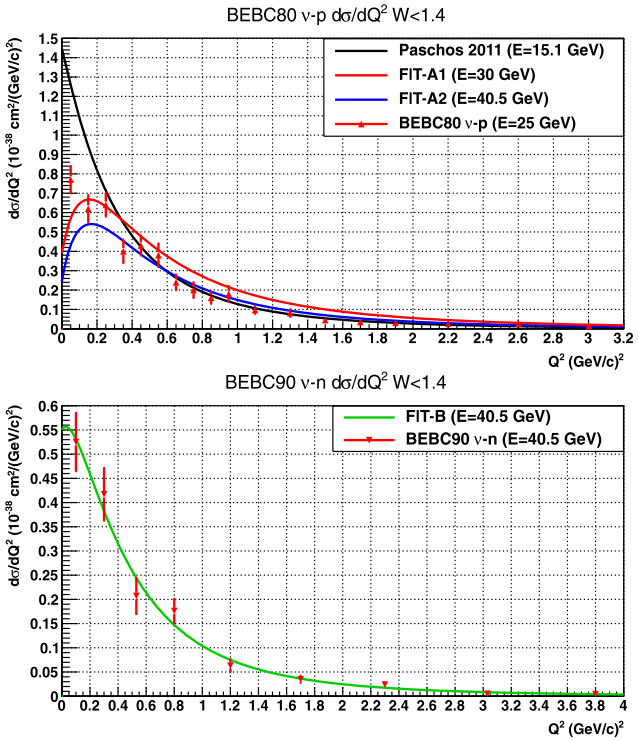

Fig. 28 *Top panel*: $d\sigma/dQ^2$ for $\nu_\mu P \to \mu^- \Delta^{++}$ cross sections (for $W < 1.4$ GeV) measured on hydrogen at high energies by Allen et al. (BEBC80 [41, 42]). *Bottom panel*: $d\sigma/dQ^2$ for $\nu_\mu N \to \mu^- \Delta^+$ cross sections (for $W < 1.4$ GeV) measured by BEBC90 on free nucleons on deuterium (Color figure online)

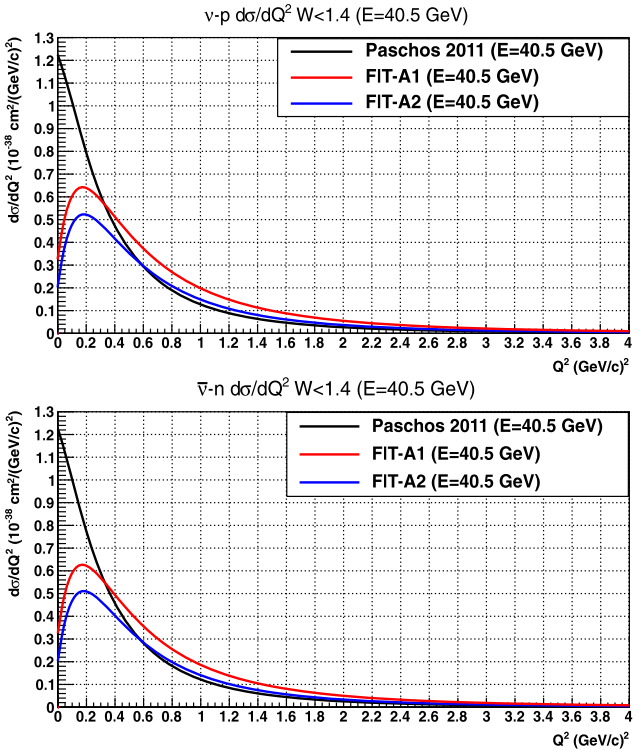

Fig. 29 The three $\nu_\mu P/\bar{\nu}_\mu N$ $d\sigma/dQ^2$ cross sections models (for $W < 1.4$ GeV) with Pauli suppression for nuclear targets at an energy of 40.5 GeV. The cross sections for $\nu_\mu P \to \mu^- \Delta^{++}$ are shown on the *top panel* and the cross sections for $\bar{\nu}_\mu N \to \mu^+ \Delta^-$ are shown on the *bottom panel* (Color figure online)

data. The variation among the three curves is taken as a systematic error.

The bottom panel of Fig. 28 shows values of $d\sigma/dQ^2$ differential cross sections for $\nu_\mu N \to \mu^- \Delta^+$ (for $W < 1.4$ GeV) measured by BEBC90 on free nucleons on deuterium. This reaction has different form factors then $\nu_\mu P \to \mu^- \Delta^{++}$. The green curve labeled FIT-B ($M_A = 1.62$, $C_5^A = 1.27$) represents a fit to the BEBC90 $\nu_\mu N$ data.

We use the above models with the addition of Pauli suppression in order to model the differential cross sections on nuclear targets.

Figure 29 shows our three $\nu_\mu P/\bar{\nu}_\mu N$ $d\sigma/dQ^2$ cross sections models (for $W < 1.4$ GeV) with Pauli suppression for nuclear targets at an energy of 40.5 GeV. The cross sections for $\nu_\mu P \to \mu^- \Delta^{++}$ are shown on the top panel and the cross sections for $\bar{\nu}_\mu N \to \mu^+ \Delta^-$ are shown on the bottom panel. These two reactions should be described by the same form factors. The black curve labeled Paschos-2011 ($M_A^\Delta = 1.05$, $C_5^A = 1.2$) is from fits to lower energy $\nu_\mu P$ free nucleon data (BNL and Argonne). The red curve labeled FIT-A1 ($M_A = 1.93$, $C_5^A = 0.62$) is from a fit to the BEBC90 $\bar{\nu}_\mu N$ free nucleon data. The blue curve labeled FIT-A2 ($M_A = 1.75$, $C_5^A = 0.49$) is from a fit to the BEBC90 $\nu_\mu P$ free nucleon data. The variation among the three curves is taken as a systematic error.

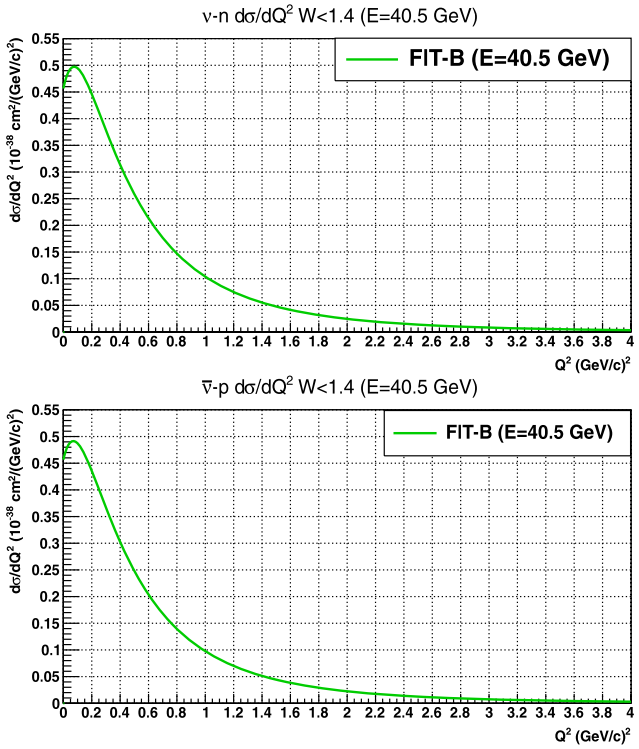

Fig. 30 Our $d\sigma/dQ^2$ cross sections model (for $W < 1.4$ GeV) with Pauli suppression for nuclear targets at an energy of 40.5 GeV. The cross sections for $\nu_\mu N \to \mu^+ \Delta^-$ are shown on the *top panel* and the cross sections for $\bar{\nu}_\mu P \to \mu^+ \Delta^0$ are shown on the *bottom panel*. The *green curve* labeled FIT-B ($M_A = 1.62$, $C_5^A = 1.27$) represents a fit to the BEBC90 $\nu_\mu N$ free nucleon data (Color figure online)

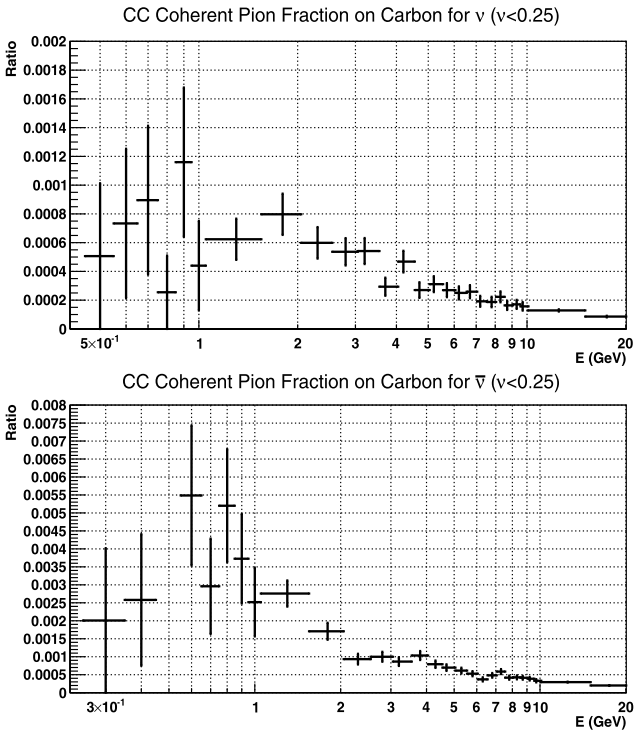

Fig. 31 The fraction of events from coherent pion production in the $\nu < 0.25$ GeV event sample (calculated with GENIE) as a function of neutrino energy: Neutrinos (*top panel*) and antineutrinos (*bottom panel*)

Figure 30 shows our $\nu_\mu N/\bar{\nu}_\mu P$ $d\sigma/dQ^2$ cross sections model (for $W < 1.4$ GeV) with Pauli suppression for nuclear targets at an energy of 40.5 GeV. The cross sections for $\nu_\mu N \to \mu^+ \Delta^-$ are shown on the top panel and the cross sections for $\bar{\nu}_\mu P \to \mu^+ \Delta^0$ are shown on the bottom panel. The green curve labeled FIT-B ($M_A = 1.62$, $C_5^A = 1.27$) is extracted fit to the BEBC90 $\nu_\mu N$ free nucleon data.

Appendix B: Coherent Pion Production

Figure 31 shows the fraction of events from coherent pion production in the $\nu < 0.25$ GeV event sample (calculated with GENIE) as a function of neutrino energy. Neutrinos are shown on the top panel and antineutrinos are shown on the bottom panel. For the $\nu < 0.25$ GeV sample, the contribution from coherent pion production is less than 0.1 % for neutrinos and less than 0.6 % for antineutrinos.

Figure 32 shows the fraction of events from coherent pion production in the $\nu < 0.50$ GeV event sample (calculated with GENIE) as a function of neutrino energy. Neutrinos are shown on the top panel and antineutrinos are shown on the bottom panel. For the $\nu < 0.50$ GeV sample, the contri-

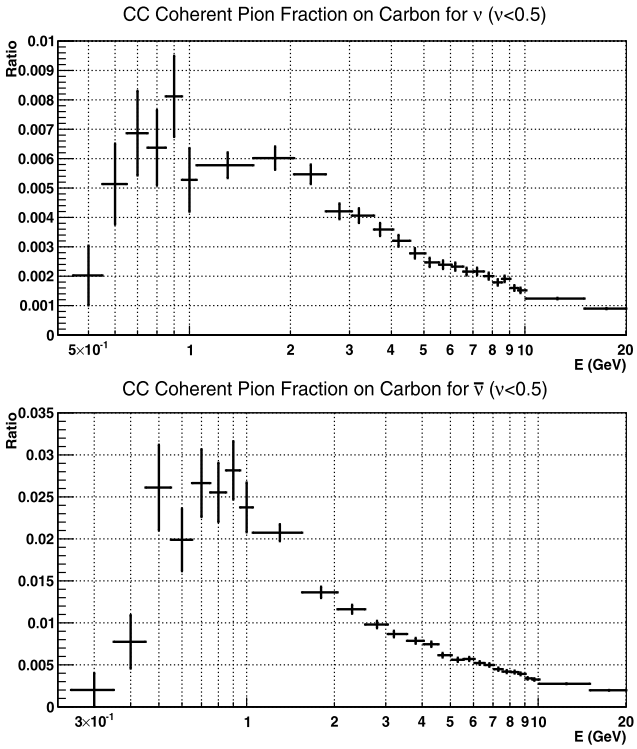

Fig. 32 Same as Fig. 31 but for the $\nu < 0.50$ GeV sample

bution from coherent pion production is less than 0.7 % for neutrinos and less than 3 % for antineutrinos.

References

1. Y. Itow et al. (T2K), arXiv:hep-ex/0106019
2. D.G. Michael et al. (MINOS), Phys. Rev. Lett. **97**, 191801 (2006). http://www-numi.fnal.gov/Minos/
3. P. Adamson et al. (MINOS), Phys. Rev. D **81**, 072002 (2010)
4. http://www-nova.fnal.gov/
5. http://minerva.fnal.gov/
6. S.R. Mishra, in *Proceedings of the Workshop on Hadron Structure Functions and Parton Distributions*, ed. by D. Geesaman et al.
7. W. Seligman, Ph.D. thesis, Columbia University, 1997, Nevis 292
8. H. Gallagher, Nucl. Phys. Proc. Suppl. **112** (2002)
9. D. Bardin, V. Dokuchaeva, Preprong JINR-E2-86-260 (1986)
10. O. Lalakulich, E.A. Paschos, Phys. Rev. D **71**, 074003 (2005)
11. O. Lalakulich, E.A. Paschos, Phys. Rev. D **74**, 014009 (2006)
12. E.A. Paschos, D. Schalla, Phys. Rev. D **84**, 013004 (2011)
13. E.A. Paschos, J.Y. Yu, Phys. Rev. D **65**, 033002 (2002)
14. C. Andreopoulos (GENIE), Nucl. Instrum. Methods A **614**, 87 (2010)
15. H. Gallagher (NEUGEN), Nucl. Phys. Proc. Suppl. **112**, 188 (2002)
16. Y. Hayato (NEUT), Nucl Phys. Proc. Suppl. **112**, 171 (2002)
17. D. Casper (NUANCE), Nucl. Phys. Proc. Suppl. **112**, 161 (2002). http://nuint.ps.uci.edu/nuance/
18. C.H. Llewellyn Smith, Phys. Rep. **3C**, 264 (1972)
19. E.A. Paschos, *Electroweak Theory* (Cambridge University Press, Cambridge, 2007)
20. A. Bodek, H. Budd, E. Christy, Eur. Phys. J. C **71**, 172 (2011)
21. F.M. Steffens, K. Tsushima, Phys. Rev. D **70**, 094040 (2004)
22. J. Carlson, J. Jourdan, R. Schiavilla, I. Sick, Phys. Rev. C **65**, 024002 (2002)
23. A. Bodek, S. Avvakumov, R. Bradford, H. Budd, Eur. Phys. J. C **53**, 349 (2008)
24. JUPITER collaboration, Jefferson Lab experiment E04-001, Arie Bodek, Cynthia Keppel and M. Eric Christy, spokespersons
25. V. Mamyan, Ph.D. dissertation, University of Virginia (2010)
26. M. Martini, M. Ericson, G. Chanfray, J. Marteau, Phys. Rev. C **80**, 065501 (2009)
27. M. Martini, M. Ericson, G. Chanfray, J. Marteau, Phys. Rev. C **81**, 045502 (2010)
28. A.A. Aguilar-Arevalo et al. (MiniBooNE), Phys. Rev. Lett. **98**, 231801 (2007)
29. A.A. Aguilar-Arevalo et al., Measurement of the neutrino component of an anti-neutrino beam observed by a non-magnetized detector. e-Print: arXiv:1102.1964 [hep-ex]
30. V. Lyubushkin et al. (NOMAD Collaboration), Eur. Phys. J. C **63**, 355 (2009)
31. Q. Wu et al. (NOMAD Collaboration), Phys. Lett. B **60**, 19 (2008)
32. V.B. Anikeev et al. (Serpukhov), Z. Phys. C **70**, 39 (1996)
33. N.J. Baker et al. (BNL), Phys. Rev. D **25**, 617 (1982)
34. J. Campbell et al. (ANL), Phys. Rev. Lett. **30**, 335 (1973)
35. S.J. Barish et al. (ANL), Phys. Rev. D **19**, 2521 (1979)
36. G.M. Radecky et al. (ANL), Phys. Rev. D **25**, 1161 (1982)
37. T. Kitagaki et al. (BNL), Phys. Rev. D **34**, 2554 (1986)
38. J. Bell et al. (FNAL), Phys. Rev. Lett. **41**, 1008 (1978)
39. J. Bell et al. (FNAL), Phys. Rev. Lett. **41**, 1012 (1978)
40. V.I. Efremenko et al. (FNAL), ITEP-83-1981 (unpublished)
41. P. Allen et al. (BEBC), Nucl. Phys. B **176**, 269 (1980)
42. P. Allen et al. (BEBC), Nucl. Phys. B **264**, 221 (1986)
43. D. Allasia et al. (BEBC), Nucl. Phys. B **343**, 285 (1990)
44. W. Lerche et al. (GGM), Phys. Lett. B **78**, 510 (1978)
45. V.V. Ammosov et al. (SKAT), Sov. J. Nucl. Phys. **50**, 57 (1988)
46. H.J. Grabosch et al. (SKAT), Z. Phys. C **41**, 527 (1989)
47. T. Bolognese et al. (GGM), Phys. Lett. B **81**, 393 (1979)
48. D. Rein, L.M. Sehgal, Ann. Phys. **133**, 79 (1981)
49. R. Belusevic, D. Rein, Phys. Rev. D **46**, 3747 (1992)
50. V.V. Ammosov et al. (FNAL E180), JETP Lett. **43**, 716 (1986)
51. V.V. Ammosov et al. (FNAL E180), Pisma Zh. Eksp. Teor. Fiz. **43**, 554 (1986)
52. J. Kiskis, Phys. Rev. D **8**, 2129 (1973)
53. R.J. Barlow, S. Wolfram, Phys. Rev. D **20**, 2198 (1979)
54. A.B. Arbuzov, D.Y. Bardin, L.V. Kalinovskaya, J. High Energy Phys. **0506**, 078 (2005). arXiv:hep-ph/0407203
55. A. De Rújula, R. Petronzio, A. Savoy-Navarro, Nucl. Phys. B **154**, 394 (1979)
56. G. Sigl, Phys. Rev. D **57**, 3786 (1998)
57. A. Bodek, Muon internal bremsstrahlung: A conventional explanation for the excess nu(e) events in MiniBoone. arXiv:0709.4004 [hep-ex]
58. E. Hernandez, J. Nieves, M. Valverde, Phys. Rev. D **76**, 033005 (2007). arXiv:hep-ph/0701149
59. O. Lalakulich, T. Leitner, O. Buss, U. Mosel, Phys. Rev. D **82**, 093001 (2010). arXiv:1007.0925
60. T. Leitner, O. Buss, L. Alvarez-Ruso, U. Mosel, Phys. Rev. C **79**, 034601 (2009). arXiv:0812.0587
61. K.M. Graczyk, D. Kielczewska, P. Przewlocki, J.T. Sobczyk, Phys. Rev. D **80**, 093001 (2009). arXiv:0908.2175
62. E. Hernandez, J. Nieves, M. Valverde, M.J. Vicente Vacas, Phys. Rev. D **81**, 085046 (2010). arXiv:1001.4416
63. L. Alvarez-Ruso, S.K. Singh, M.J. Vicente Vacas, Phys. Rev. C **59**, 3386 (1999). arXiv:nucl-th/9804007
64. M. Sajjad Athar, S. Chauhan, S.K. Singh, J. Phys. G **37**, 015005 (2010). arXiv:0908.1442
65. G.M. Radecky et al., Phys. Rev. D **25**, 1161 (1982)